Recent results on elastic and inelastic scattering

N. Alamanos, P. Roussel-Chomaz

CEA/SACLAY
DSM

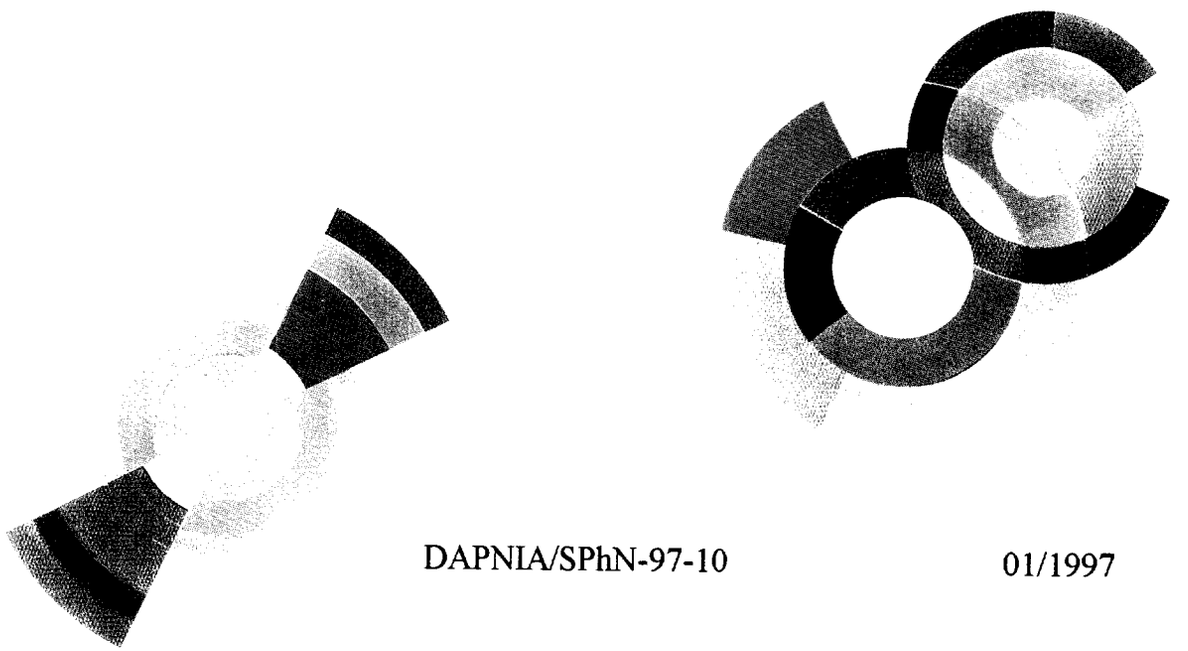

DAPNIA/SPhN-97-10 01/1997

Recent results on elastic and inelastic scattering

N. Alamanos and P. Roussel-Chomaz

DAPNIA

Département d'**A**strophysique, de Physique des **P**articules, de Physique **N**ucléaire et de l'**I**nstrumentation **A**ssociée
CEA/Saclay F-91191 Gif-sur-Yvette Cédex

Couverture : Sylvie Cabrit et Marc Sauvage

Submitted to Annales de Physique

RECENT RESULTS ON ELASTIC AND INELASTIC SCATTERING

N. Alamanos[1] and P. Roussel-Chomaz[2]

1) CEA/DSM/DAPNIA/SPhN Saclay,91191 Gif-sur-Yvette Cedex, France
2) GANIL (DSM/CEA, IN2P3/CNRS), BP 5027, 14021 Caen Cedex, France

« Theories come and go, but fundamental
data always remain the same »
Mary Nicol Leakey: 1913-1996

Abstract

In this review article, which corresponds to lectures given by one of us (N.A) at the third « Euroschool on Exotic Beams » held in Leuven in September 1995, we present experimental results and theoretical developments in heavy-ion elastic and inelastic scattering and Giant Resonance excitation. The paper contains a short review of the field with special emphasis on more recent results and problems. We start by recalling the theoretical situation concerning the description of nucleon-nucleus elastic scattering. We show that in the framework of the local density approximation, complex potentials derived from fundamental effective nucleon-nucleon interactions, describe successfully the data. However, the main part of the discussion on elastic scattering, is dedicated to the description of intermediate energy heavy-ion elastic scattering. We present different folding models for the calculation of the real part of the nucleus-

nucleus optical potential, M3Y, DDM3Y,.... The theoretical predictions are compared to experimental data mainly obtained at GANIL. We show that a new density dependent interaction which reproduces the equilibrium density and the binding energy of normal nuclear matter, leads also to a satisfactory description of heavy-ion elastic scattering angular distributions. This interaction reproduces also the density and energy dependence of the nucleon optical potential. We present a new simple effective interaction with a real and imaginary part for peripheral heavy-ion collisions at intermediate energies. Finally the effect of the isospin and spin terms of the effective nucleon-nucleon interaction on the nucleus-nucleus folded potentials is discussed.

We introduce the deformed optical model potential which is the most frequently used model, to obtain inelastic scattering transition potentials. However the most direct approach to obtain transition potentials is from the folding of the transition densities with an effective nucleon-nucleon interaction and the ground state density of the nucleus which is not excited. We show that the predictions of the optical and folding model are very different, especially for transitions dominated by nuclear excitation. The difference between the cross sections estimated within the deformed optical model and the folding model increases with multipolarity. Following the theoretical work of R. Satchler, we recommend the use of a folding model to extract deformation lengths and multipole moments from inelastic scattering measurements.

We present the state of the field concerning Electric Giant Resonances and multiphonon excitations. We introduce the different sum rules which can be found usually in the literature and we show the link between them. The excitation of Giant Resonances with intermediate energy or high energy heavy ions, measured at GANIL or GSI and the technical problems met in the analysis of these experiments are discussed. Recent results concerning the two-phonon excitation of the Giant Quadrupole and Dipole mode are presented. Concerning the breathing mode, macroscopic and microscopic prescriptions introduced to access the compressibility of the nuclear matter are discussed. We show, in the light of theoretical arguments developed recently by J.P. Blaizot and collaborators, that microscopic calculations remain the most reliable tool for the determination of the nuclear matter compression modulus from the energy of the monopole vibration of nuclei.

CONTENTS

1. OPTICAL MODELS AND ELASTIC SCATTERING

1-1. INTRODUCTION

1-2. NUCLEON-NUCLEUS ELASTIC SCATTERING

1-3. NUCLEUS-NUCLEUS ELASTIC SCATTERING

1-3-a) The nuclear densities

1-3-b) The M3Y effective interaction and its density dependent versions

1-3-c) A new simple effective interaction for peripheral heavy-ion collisions at intermediate energies

1-3-d) Isospin and spin dependence of the effective nucleon-nucleon interaction

1-3-e) Study of elastic scattering induced by light unstable nuclei

2. INELASTIC SCATTERING

2-1. THE DISTORTED WAVE BORN APPROXIMATION

2-2. THE DEFORMATION PARAMETERS

2-3. EXAMPLES OF INELASTIC SCATTERING

Excitation of the 2^+ state in ^{208}Pb by $^{17}O+^{208}Pb$ inelastic scattering

Excitation of the 3^- state in ^{208}Pb by $^{17}O+^{208}Pb$ inelastic scattering

Excitation of the 2^+ state in ^{32}Mg by $^{32}Mg+^{208}Pb$ inelastic scattering

2-4. THE FOLDING MODEL FOR DISCRIBING INELASTIC SCATTERING

3. ELECTRIC GIANT RESONANCES

3-1. PHENOMENOLOGY

3-2. THE GIANT DIPOLE RESONANCE

3-3. THE GIANT QUADRUPOLE RESONANCE
3-4. THE GIANT MONOPOLE RESONANCE

OUTLOOK

1. OPTICAL MODELS AND ELASTIC SCATTERING

1-1. INTRODUCTION

The optical model is the simplest and most successful model to describe the scattering of nuclei. It describes the interaction of two nuclei in terms of a potential. The interaction of two nuclei (even if one of them is a single nucleon) is a complicated many body problem. For the purpose of describing elastic scattering, the optical model attempts to replace this problem by the much simpler one of two structureless bodies interacting via a simple potential $U(\vec{r}_\alpha)$. Except for a possible dependence on the spins of the two nuclei, this potential is usually assumed to depend only upon the distance $\vec{r}_\alpha$ between the centers of mass of the two nuclei. Whenever non-elastic scattering is possible, there is a loss of flux from the elastic channel. Hence the optical potential must be absorptive. This is accomplished by making the potential complex.

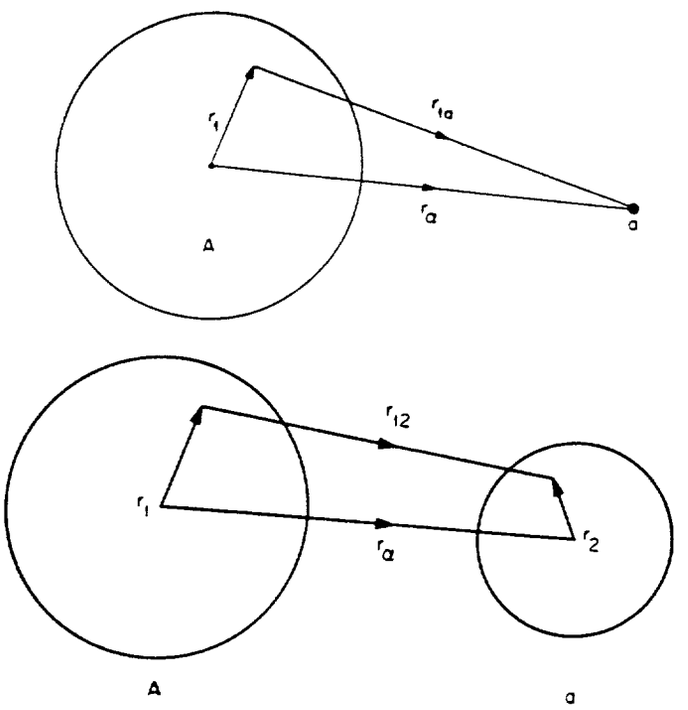

Fig.1.1 Coordinates used for (a) single-folding, and (b) double folding [Sa83]

If an incident nucleon α interacts with each target nucleon i through a nucleon-nucleon potential, or effective interaction $u(|\vec{r}_a - \vec{r}_1|)$, where $|\vec{r}_a - \vec{r}_1|$ is the distance between them, (see Fig.1.1), then the overall potential it experiences due to the target nucleus is

$$U(\vec{r}_\alpha) = \int \rho_A(\vec{r}_1) u(\vec{r}_a - \vec{r}_1) d\vec{r}_1 \qquad (1.1)$$

where $\rho_A(\vec{r}_1)$ is the density of the nucleus A at the position i. The nucleon-nucleon effective interaction has a short range and therefore for separation distances greater than about 1 fm it decreases exponentially. Hence when folded into the nuclear density distribution, the resulting potential has a shape which loosely follows $\rho_A(\vec{r}_1)$ but with a more rounded surface (Fig.1.2).

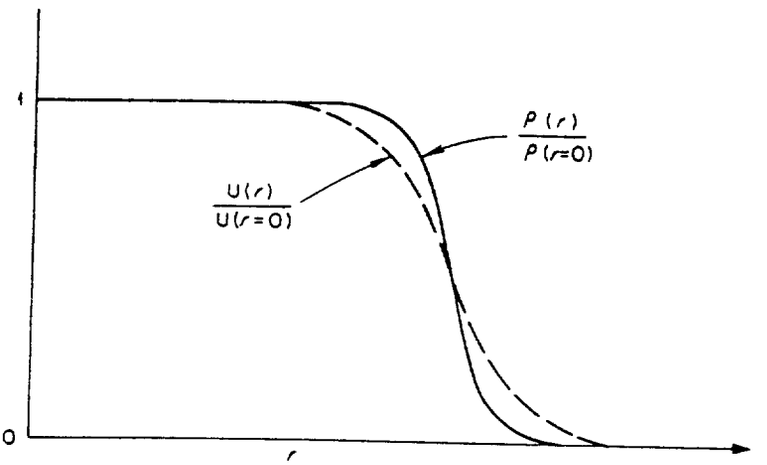

Fig.1.2 Comparison between the shape of a density distribution and the potential obtained by folding it with a short-ranged interaction [Sa83].

The potential (1.1) describes the scattering of two particles, where the target is undisturbed and elastic scattering is the only possible process. But other reaction channels are possible and their existence affects the elastic scattering. For example, an incident nucleon may excite the target nucleus which then deexcite and the system does not return to the entrance channel. If an excitation of this type takes place, we have a non-elastic event. The projectile is then lost from the entrance channel and may be thought of as being absorbed. If we are not interested in the details of the non elastic

process, but only in their effect on the elastic scattering, we can represent this absorption by adding an imaginary term to the optical potential.

In the same way as for nucleons, potentials for composite projectiles like deuterons, α-particles and heavier ions can be constructed. In this case we must integrate over the nucleons in the projectile as well as in the target. If the density distribution in the target is $\rho_A(\vec{r})$ and that in the projectile is $\rho_a(\vec{r})$, equation (1.1) is replaced by the following formula

$$U(\vec{r}_a) = \iint \rho_A(\vec{r}_1)\rho_a(\vec{r}_2)u(\vec{r}_{12})d\vec{r}_1 d\vec{r}_2 \tag{1.2}$$

where $\vec{r}_{12} = \vec{r}_a - \vec{r}_1 + \vec{r}_2$. The folding expressions (1.1) and (1.2) are easy to evaluate. If we work in momentum space the double-folding reduces to a product of three Fourier transforms while the single-folding reduces to a product of two transforms (§1.3). Clearly the additional integration over the projectile distribution will lead to a potential much like that of eq. (1.1) but with an even more diffuse surface.

There are two important ingredients in the calculation of the above potentials (eq. (1.1) and eq. (1.2)), the effective nucleon-nucleon interaction and the density distribution of the colliding nuclei. The central part of the effective interaction may be written as:

$$u = u_{00} + u_{01}\vec{\tau}_1\vec{\tau}_2 + u_{10}\vec{\sigma}_1\vec{\sigma}_2 + u_{11}\vec{\tau}_1\vec{\tau}_2\vec{\sigma}_1\vec{\sigma}_2 \tag{1.3}$$

For calculating the effective nucleon-nucleon interaction the most popular approach parallels that used in the nuclear shell model. In it, one calculates the scattering of two nucleons while they are embedded in nuclear matter of various densities. The nuclear medium provides an average potential in which the nucleons move, allows propagation off the energy shell and, through the Pauli principle, modifies the scattering by blocking intermediate virtual states that are occupied by other nucleons [Sa83]. The Bethe-Golstone equation for this scattering problem is solved, yielding a density-dependent reaction or G-matrix (an extensive discussion on Bethe-Goldstone equation and G-matrix, can be found in [Pr75]). The G-matrix so obtained is still a complicated object, and attempts have been made to find simple representations that are easier to use in spectroscopic applications, that is by generating simple

mathematical formulae which reproduce the G-matrix elements. In an approach, appropriate for low energies [Be77], the G-matrix for scattering of one nucleon by a bound nucleon was assumed to be very close to that for two bound nucleons. The effective interaction was represented by a sum of Yukawa functions (M3Y interactions), the strengths of which were adjusted to reproduce the G-matrix elements.

From their origin in G-matrices for bound nucleons, M3Y effective interactions are real and have to be supplemented by phenomenological imaginary parts. In addition, they contain no explicit density dependence or energy dependence. These deficiencies have been rectified in density and energy dependent calculations of the G-matrix. J.P.Jeukenne et al. [Je77], starting from the Bruekner-Hartree-Fock approximation and Reid's hard core nucleon-nucleon interaction have calculated and parametrized the energy- and density dependence of the isoscalar, isovector and Coulomb components of the complex optical potential.

A discussion of the different methods applied for obtaining the « microscopic » nucleon-nucleon interaction is lengthy and goes beyond the scope of the present article. We would like to insist on the fact that « microscopic » approaches denote attempts to understand the scattering in terms of the motions of individual nucleons and their interactions instead of using phenomenological, one-body potential models. In that sense folding models incorporate more nuclear structure information than phenomenological approaches.

The second important ingredient in these calculations is the density distribution of the colliding nuclei. The most direct measure we have of the densities, to be used in equations (1.1) and (1.2), comes from electron scattering. This yields information about the charge density and hence primarily about the proton distribution. However, for light nuclei with N=Z, it is not unreasonable to assume that the neutron and proton distributions are the same. Average expressions, of Fermi shape, of the proton and neutron density distributions were proposed some years ago by Negele, [Ne70].

$$\rho^{(k)}(r) = \frac{\rho_0^k}{1+\exp[(r-c_\rho)/a_\rho]} \qquad (1.4)$$

where $a_\rho = 0.54$

$$c_\rho = (0.978 + 0.0206A^{1/3})A^{1/3} \quad \text{and} \quad \rho_0^k = \frac{3k}{4\pi(1+\pi^2 a_\rho^2/c_\rho^2)}$$

k = N or Z. This parametrization reproduces reasonably well the experimental charge density distribution, its accuracy is poorer however for light nuclei.

For unstable nuclei, for which the densities are obviously not known from electron scattering experiments, theoretical density distributions have to be used. Analysis using folded potentials for nucleon-nucleus and nucleus-nucleus elastic and inelastic scattering will be presented in §1.2 and §1.3.

The short range of the nucleon-nucleon interaction implies that the shape of the potentials resulting by folding the nucleon-nucleon interaction with a density distribution loosely follows the shape of the density distribution. In that sense equation (1.4) justifies a posteriori the use of phenomenological potentials of Woods-Saxon form which have been widely used to study the dynamics of elastic scattering. The real part of these optical potentials is given by the expression:

$$U(r) = V_0 / (1 + \exp((r - R_v) / \alpha_v)) \tag{1.5}$$

where V_0, R_v and a_v are known as the well-depth, radius, and diffuseness respectively, similar expressions are used for the imaginary and the spin orbit part of the nuclear potential. Analysis using phenomenological potentials for describing nucleon-nucleus and nucleus-nucleus elastic and inelastic scattering have been presented in many publications.

To study the sensitivity of the elastic and inelastic scattering angular distributions with respect to the nuclear potential (elastic scattering) and to the transition potential (inelastic scattering) the data are usually confronted to the predictions of the optical model and to the predictions of the distorted-wave Born approximation (DWBA).

The differential cross section for elastic scattering from the potential U(r) can be expressed directly in terms of the scattering amplitude $f(\theta)$, $\frac{d\sigma}{d\Omega} = |f(\theta)|^2$ where the scattering amplitude is given by the expression

$$f(\theta) = \frac{1}{k}\sum_{l=0}^{\infty}(2l+1)e^{i\delta_l}\sin\delta_l P_l(\cos\theta) \tag{1.6}$$

where δ_l is called the phase shift and is related to the asymptotic behavior of the radial wave function $u_l(r)$:

$$u_l(r)_{r\to\infty} \approx e^{i\delta_l} \sin(kr - \frac{l\pi}{2} + \delta_l) \tag{1.7}$$

solution of the Schrondinger equation

$$\frac{d^2u_l}{dr^2} + \left[\frac{2m}{\hbar^2}(E - U(r)) - \frac{l(l+1)}{r^2}\right]u_l = 0 \tag{1.8}$$

Many codes are available today, ECIS [Ra81], PTOLEMY [Rh80], FRESCO [Th88],....which can be used to perform these calculations. In the next chapters we shall mainly focus our attention on the origin of the optical and transition potentials parameters, rather than on technical details concerning the codes.

1-2. NUCLEON-NUCLEUS ELASTIC SCATTERING

Elastic neutron and proton scattering from nuclei is most frequently described in terms of complex optical potential models. These are often phenomenologically based, using standard form factors for the potential wells, with the depths and geometries determined by fitting experimental data [Va91]. However, the potentials can be derived from the more fundamental effective nucleon-nucleon interaction by applying folding integrals [Ge89]. Microscopic optical potentials derived from both the nuclear matter calculation of Jeukenne, Lejeune, and Mahaux [Je77], and the energy and density dependent t matrix of Brieva and Rook [Br78] have been successful in describing nucleon scattering from medium and heavy nuclei [Me83]. The extension of these calculations to light nuclei constitutes a severe test of the applicability of the local density approximation that is used to obtain optical potentials for finite nuclei from calculations performed in « infinite nuclear matter ». The spherical potential derived from the work of Jeukenne, Lejeune, and Mahaux (JLM) provides also a consistent description of differential cross sections of nucleon scattering from light nuclei whereas the interaction of Brieva and Rook (BRVG) gives less satisfactory agreement [Pe85]. The starting point for computing JLM potentials, is the Brueckner-Hartree-Fock approximation and the Reid hard core nucleon-nucleon interaction which provide, for energies up to 160 MeV, the energy and density dependence of the isoscalar, isovector and Coulomb components of the complex optical model potential in infinite nuclear matter. In order to provide the reader with usable expressions, Jeukenne, Lejeune, and Mahaux have parametrized their numerical results for the real and imaginary parts in an analytical form. For instance, the real part of the optical model $V_0(\rho,E)$ potential is given by the expression:

$$V_0(\rho,E) = \sum \alpha_{ij} \rho^i E^{j-1} \qquad (1.9)$$

The coefficients α_{ij} are tabulated in [Je77]. The choice of the powers of ρ appearing in Eq.(1.9) is largely arbitrary. The only physical requirement is that for small densities the potential $V_0(\rho,E)$ must become proportional to the probability of having another nucleon in the neighborhood of the incident particle. The expression (1.9) has

been fitted to the calculated values of $V_0(\rho,E)$ in the energy interval $10 \le E \le 160$ MeV.

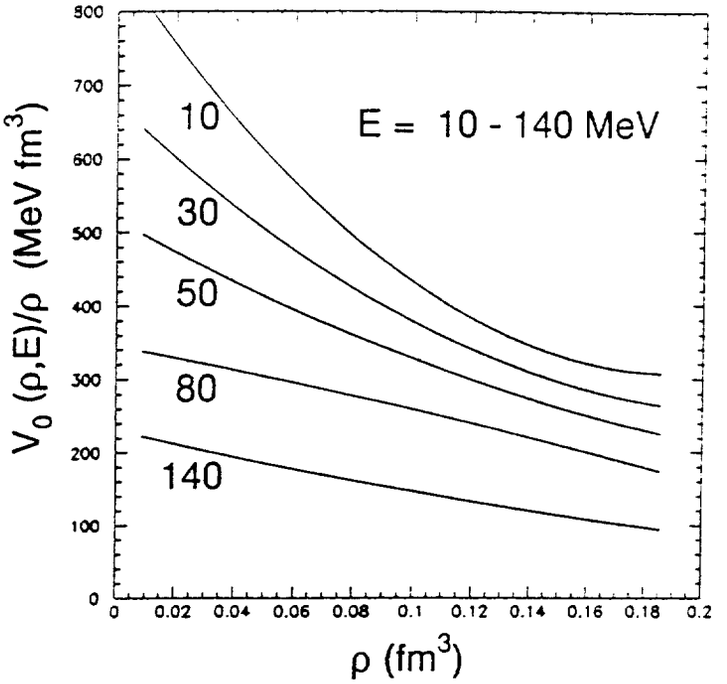

Fig.1.3 Dependence on density and energy of the quantity $V_0(\rho,E)/\rho$

As an example of these calculations Fig.3.1 shows the behavior of the strength of the ratio $V_0(\rho,E)/\rho$ in infinite nuclear matter versus ρ, where ρ is the nuclear density $\rho = 2K_F^3/(3\pi^2)$, and K_f denotes the Fermi momentum. This ratio decreases with increasing energy and increasing density.

The optical potential of a finite nucleus is obtained by applying equation (1.9) but with ρ(r) the density distribution of the nucleus.

$$V_E(r) + iW_E(r) = V(\rho(r),E) + iW(\rho(r),E) \qquad (1.10)$$

This approximation is known as the local density approximation [LDA]. The local density approximation provides root mean square radii, for different nuclei which are too small. This was ascribed to the fact that the local density approximation does not include accurately the effect of the range of the effective interaction. This was included in a phenomenological way by convoluting the potential obtained in the local density

approximation with a Gaussian form factor ~exp(-(r/t)^2). The range parameter t was chosen equal to 1.2 fm in the original work of [Je77].

$$\overline{V}_E(r) = (t\sqrt{\pi})^{-3} \int V(\rho(r'), E) \exp(-|\vec{r} - \vec{r}'|^2 / t^2) d^3r' \qquad (1.11)$$

The JLM central potential has been extensively studied by S. Mellema et al. [Me83] and J.S. Petler et al. [Pe85]. It has been particularly successful in describing elastic neutron and proton scattering from stable nuclei, provided the imaginary potential is adjusted slightly by a normalization factor of the order of λ_w~0.8. A finite range parameter of the nuclear force t of 1.0 fm for both the real and the imaginary potentials, has been proved to yield better results than the initial value of t=1.2 fm. These calculations require the nuclear ground state matter densities as input. The proton point-nucleon density ρ_p is obtained by unfolding the proton charge distribution from the charge density measured by electron scattering. The neutron density ρ_n is assumed to be the same as for protons for the N=Z nuclei and, in others cases, was determined by applying the assumption ρ_n=(N/Z)ρ_p. Fig. 1.4 show for neutron scattering on ^{16}O at 26MeV, the results of three separate JLM calculations for different values of λ_w and shows the sensitivity of these calculations to small variations of the depth of the imaginary potential [Tr94]. Fig.1.5 was adapted from [Pe85] and shows the results of JLM and BRVG microscopic calculations for ^{13}C(n,n) and ^{13}C(p,p) elastic scattering at a number of energies between 10 and 35 MeV. It is obvious that the JLM results provide a better description of the experimental data than the BRGV results, which for ^{13}C(n,n) overpredict the measured cross sections at forward angles and lie under the data at larger angles. The JLM central potential has been particularly successful in describing elastic neutron and proton scattering from many light and intermediate mass nuclei.

We extended these calculations in the case of unstable nuclei. In all cases, we will use a renormalization factor λ_w=0.8 for the imaginary part and a range parameter t=1.0 fm as was done for stable nuclei. The density distribution of ^{11}Li is presented in the upper part of Fig.1.6. It was provided by the relation [Be78]:

$$\rho_{p,n}(r) = \sum_{p,n} |\psi(r)|^2 \qquad (1.12)$$

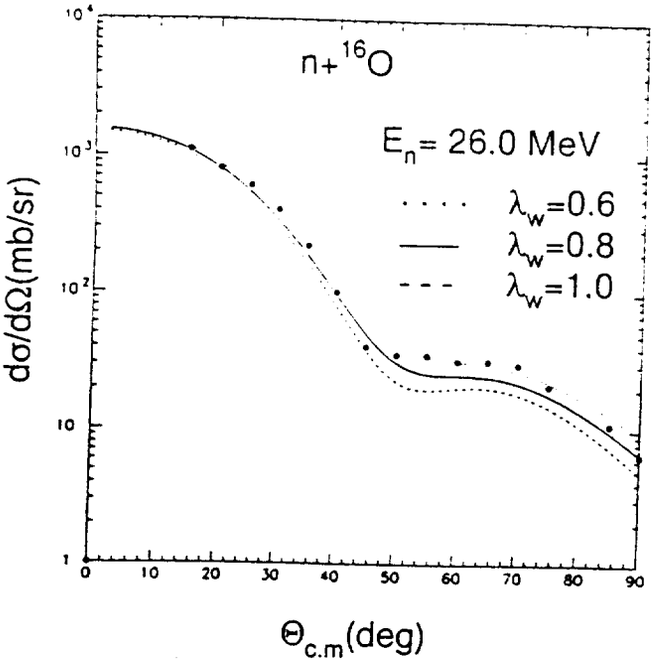

Fig.1.4 Elastic scattering angular distribution for n+^{16}O for different values of the imaginary potential.

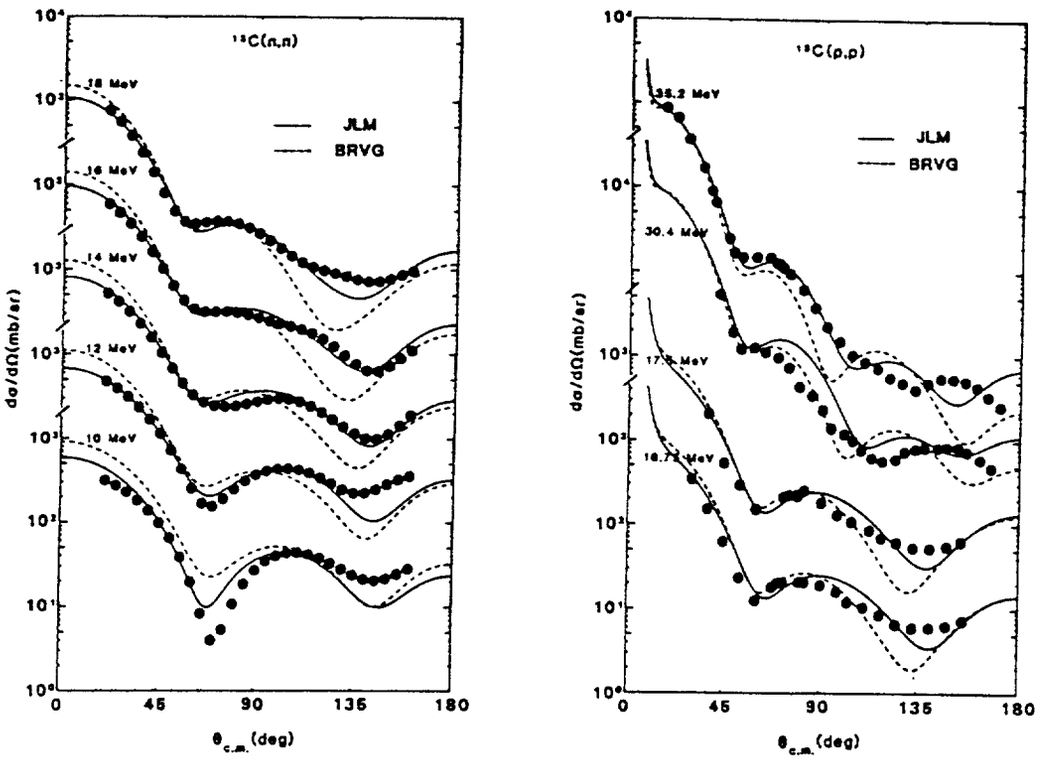

Fig.1.5 Fits obtained with JLM and BRGV calculations for proton and neutron scattering from ^{13}C.

where $\psi(r)$ is the eigenfunction of protons and neutrons (p,n) bound in a potential well and depends on the binding energy of the particles in the well.

The solid line presents the result of a calculation for a two-neutron separation energy of ^{11}Li of the order of 0.500 MeV in agreement with the experimental results [Ta88], [Fu91], whereas the dotted line corresponds to a calculation for a separation energy of the order of 10 MeV.

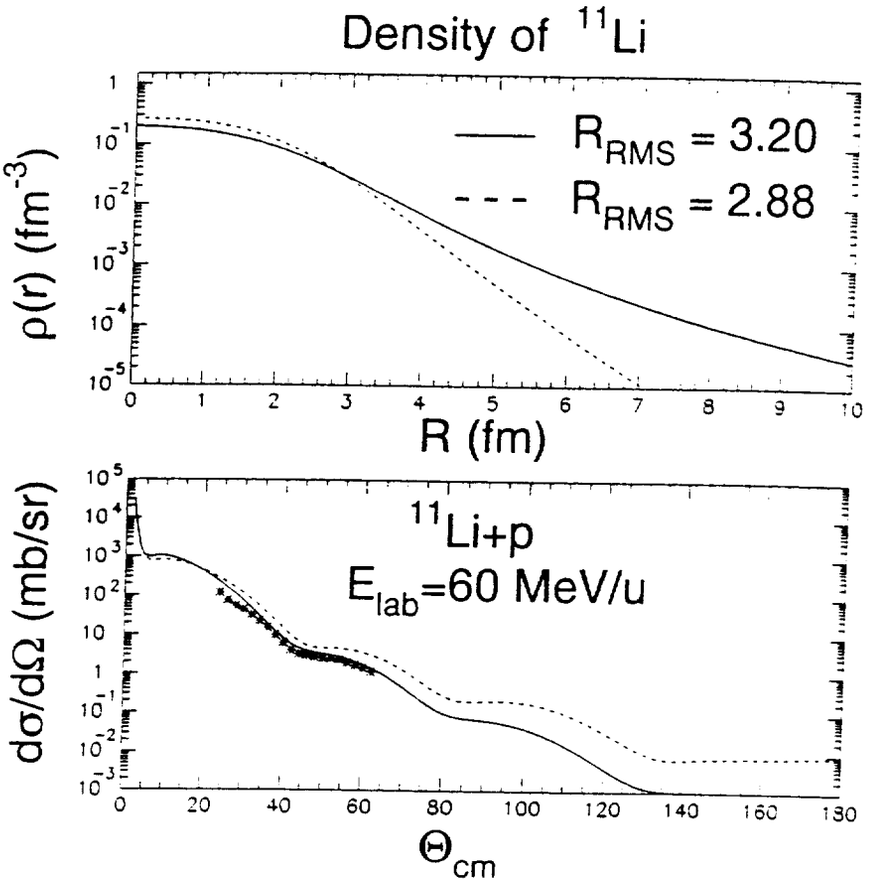

Fig. 1.6 (upper part) Density distributions of ^{11}Li corresponding to two different values of the rms radius. (lower part) JLM calculations for the system ^{11}Li-p at 60MeV nucleon for the two density distributions.

The root mean square radii corresponding to these two density distributions are 3.20 fm and 2.88 fm respectively. The value of 3.20 fm is in qualitative agreement with the experimental value of the root mean square radius of ^{11}Li of 3.16 fm, whereas the value of 2.80 is a typical value for the interaction radius of light, not halo, unstable nuclei in

the A=11,12 mass region [Ta88]. The solid and dotted lines in the lower part of Fig.1.6 are the results of JLM calculations for the system ^{11}Li+p at 60MeV/nucleon and for the two density distributions presented in the same figure. The two calculations are compared to the experimental data obtained by Moon et al. [Mo92]. The experimental results are in better agreement with a calculation using a nuclear matter density distribution with a long tail and a root mean square radius of 3.20 fm. Very recently the ^{11}Li density distribution was calculated by J. Dechargé and J. F. Berger [De95]. In their many-body calculations the only input is the well tested, finite-range D1S effective interaction of Gogny. Pairing correlations are included in a constrained Hartree-Fock-Bogolyubov (HFB) calculation. The resulting density distribution is shown in the upper part of Fig.1.7 (dotted line).

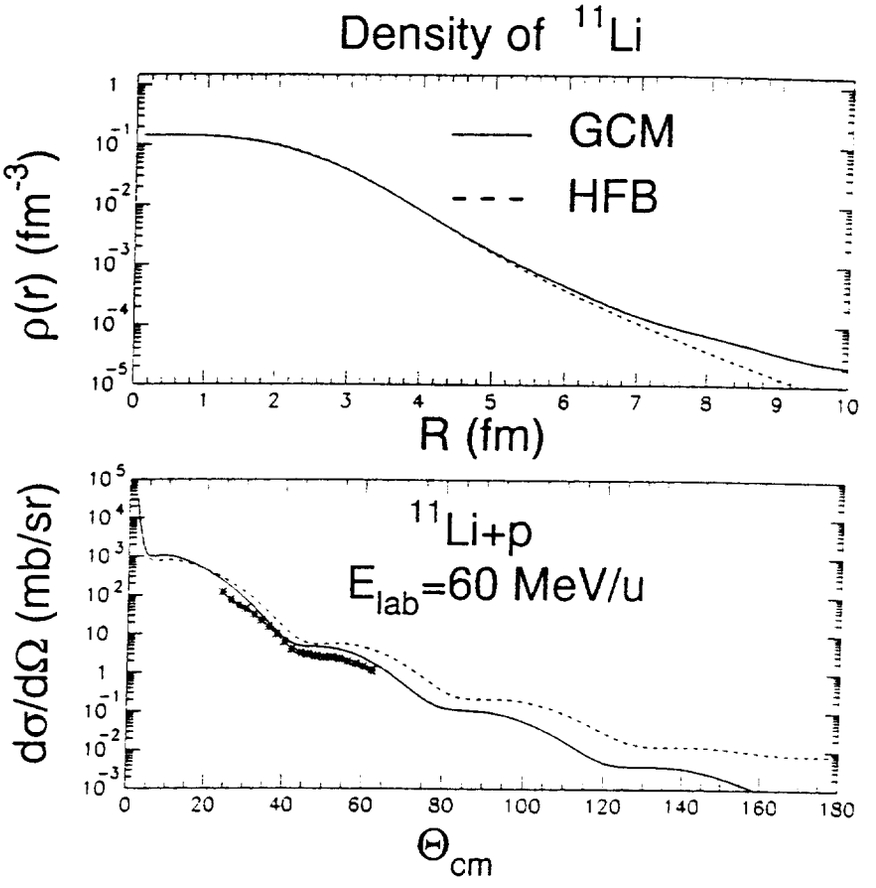

Fig.1.7 (upper part) Density distributions of ^{11}Li within HFB and GCM approaches. (lower part) JLM calculations for the system ^{11}Li-p at 60MeV nucleon for the two density distributions.

HFB calculations do not take into account long range collective correlations which may be important in the case of halo nuclei, since loosely bound neutrons can occupy orbits having a broad range of radial extension. Long-range collective correlations were introduced by using a Generator Coordinate Method (GCM) type formalism. The resulting density distribution is shown in the upper part of Fig.1.7. The mean square radii of the ^{11}Li nuclear matter density distribution for the HFB and GCM calculations are 2.80 fm and 3.42 fm respectively. These microscopic density distributions were also introduced in the JLM code to calculate the ^{11}Li+p angular distributions. The results of these calculations are shown in the lower part of Fig.1.7. The JLM calculation with the GCM density distribution is in better agreement with the experimental data than the calculation using the HFB density distribution. It is therefore clear from these different analyses that the parameter-free JLM calculations may reproduce proton plus unstable nucleus elastic scattering, when a 'realistic' nuclear matter density distribution is used. Certainly this type of JLM calculations have to be extended to other measurements involving other unstable nuclei and in that sense the conclusion drawn from this ^{11}Li+p elastic scattering analysis have to be considered as « preliminary ».

In a recent work we have measured proton-nucleus elastic scattering angular distributions for ^{6}He, ^{7}Li, ^{10}Be and ^{11}Be secondary beams. These data, together with proton-nucleus elastic scattering angular distributions for ^{8}He, ^{9}Li and ^{11}Li measured by [Ko93] and [Mo92], were analyzed using the standard phenomenological optical potential [Va91] and within the framework of the JLM model. In order to best reproduce the data, the real potential has to be decreased and the imaginary potential increased for all nuclei, except ^{7}Li for which the standard potentials give satisfactory results. The fact that very similar renormalizations are necessary for two different potentials, a phenomenological one and a microscopic one, where the halo is explicitly included, indicates that the trend observed is not model dependent. Such renormalizations would appear to be related to the break-up processes which should be important for loosely bound light nuclei.

One of the ultimate goal of these studies is to obtain information on nuclear densities. To achievement of this goal pass through a theoretical description of break-up processes in proton plus nucleus elastic scattering.

1-3. NUCLEUS-NUCLEUS ELASTIC SCATTERING

During the last decade, the double folding model has been widely used by many groups to describe the heavy ion scattering, due probably to its simple handling in numerical calculations. In this model the potential is obtained by folding the distributions $\rho_i(\vec{r})$ of the centers of mass of the nucleons in the ground state of the two interacting nuclei with an effective nucleon-nucleon interaction $u(\vec{r}_{12})$ (see eq.1.2)

Because of the integration over two densities, this is often called the double-folding model. The expression (1.2) involves a six-dimensional integral. However, it is quite simple to evaluate in the momentum space where it reduces to a product of three one dimensional integrals. If we denote the Fourier transform of a function $f(\vec{r})$ by:

$$\tilde{f}(\vec{k}) = \int d\vec{r} \exp(-i\vec{k}\vec{r}) f(\vec{r}) \tag{1.13}$$

then

$$f(\vec{r}) = (2\pi)^{-3} \int d\vec{k} \exp(i\vec{k}\vec{r}) \tilde{f}(\vec{k}) \tag{1.14}$$

In the case of $u(\vec{r}_{12})$, one gets

$$u(\vec{r}_{12}) = (2\pi)^{-3} \int d\vec{k} \tilde{u}(\vec{k}) \exp(i\vec{k}(\vec{R} + \vec{r}_2 - \vec{r}_1)) \tag{1.15}$$

and

$$U_F(\vec{r}) = (2\pi)^{-3} \int d\vec{r}_1 \int d\vec{r}_2 \rho_A(\vec{r}_1) \rho_a(\vec{r}_2) \tilde{u}(\vec{k}) \exp(i\vec{k}(\vec{R} + \vec{r}_2 - \vec{r}_1)) d\vec{k}$$

$$= (2\pi)^{-3} \int \tilde{\rho}_A(\vec{k}) \tilde{\rho}_a(-\vec{k}) \tilde{u}(\vec{k}) \exp(i\vec{k}\vec{R}) d\vec{k} \tag{1.16}$$

Therefore

$$\tilde{U}_F(\vec{k}) = \tilde{\rho}_A(\vec{k}) \tilde{\rho}_a(-\vec{k}) \tilde{u}(\vec{k}) \tag{1.17}$$

The Fourier transform of (1.17) provides the optical potential in r space.

The original version of the folding model which was based on the M3Y effective nucleon-nucleon interaction, seems to deliver satisfying results in most cases where the heavy ion interaction is dominated by strong absorption, i.e., when the elastic-scattering data are sensitive to the heavy ion optical potential only in the surface region. However,

it is well established now that in certain cases, where the data are sensitive to the optical potential over a wider radial domain, the simple double folding model fails to give a good description of the data [Sa79]. Therefore, some further developments of the folding model have been made to obtain more realistic shape of the folded potential. One of the approaches is to apply on the M3Y interaction, an explicit density dependence to account explicitly for the in-medium effects which are more substantial at small internuclear distances. The resulting interaction is the density dependent M3Y interaction (DDM3Y) [Az85]. Recently the double-folding model was generalized for the calculation of the nucleus-nucleus potential using a new version of the density-dependent M3Y interaction which reproduces consistently the equilibrium density, and binding energy of normal nuclear matter as well as the density- and energy dependence of the nucleon optical potential [Kh94]. However all these approaches suffer from the fact that the imaginary potential is treated in a phenomenological way. To overcome this difficulty R. Satchler has proposed a new simple nucleon-nucleon interaction which is appropriate for peripheral collisions (no density dependence) at intermediate energies [Sa94].

In this chapter we shall describe briefly these models and compare some experimental elastic scattering angular distributions to the theoretical predictions.

1-3-a) The M3Y effective interaction and its density dependent versions

The oldest and most popular effective interaction is the M3Y interaction. In the M3Y approach the u_{00} and u_{01} components of equation (1.3) have the form

$$u_{00}(r) = \left[7999 \frac{e^{-4r}}{4r} - 2134 \frac{e^{-2.5r}}{2.5r} \right] \text{MeV} \qquad (1.18)$$

and

$$u_{01}(r) = -\left[4886 \frac{e^{-4r}}{4r} - 1176 \frac{e^{-2.5}}{2.5r} \right] \text{MeV} \qquad (1.19)$$

The form (1.18) and (1.19) is not antisymmetrised for the nucleons in different nuclei, but the individual wavefunctions for nuclei a and A are themselves assumed antisymmetric. The dominant correction arising from antisymmetrisation will be the single-nucleon exchange, which for nucleon-nucleus scattering has been called "knock-

on exchange". This term is included formally in the double folding integral by replacing $u(\vec{r}_{12})$ by (1-P_{12}) $u(\vec{r}_{12})$, where P_{12} exchanges all the coordinates of nucleons 1 and 2. It has been found that the effect of the single nucleon exchange can be estimated by replacing -$P_{12}\,u(\vec{r}_{12})$ by the pseudopotential $j(E)\delta(\vec{r}_{12})$. The strength j(E) of the pseudo-potential associated with the term u_{00} is $j(E) \approx 276(1 - 0.005E/A)$ MeV fm^3 and the effective interaction becomes,

$$u_{00}(r,E) = \left[7999\frac{e^{-4r}}{4r} - 2134\frac{e^{-2.5r}}{2.5r} - 276(1 - 0.005E/A)\delta(\vec{r}) \right] \text{ MeV} \tag{1.20}$$

The folding model with a properly chosen effective interaction, the M3Y interaction, has been successful in reproducing the scattering of many systems with bombarding energies in the range of 5 to 20 MeV per nucleon [Sa79]. The real potentials for these systems are given correctly if the calculated folded potentials are renormalized by a factor N where $N = 1.11 \pm 0.13$. The only exceptions established so far (for stable nuclei) occurs for the scattering of ^{6}Li and ^{9}Be which require a reduction in the strength of the calculated folded potential by a factor of about two [Sa79]. In the case of ^{6}Li this effect was shown, by a complete coupled-channels reaction model, to be due to the breakup of this loosely bound nucleus. The breakup effect can be represented by a dynamical polarization potential which has a strongly repulsive real part in the surface, and an additional absorptive (imaginary) part [Sa86].

The M3Y interaction contains no explicit density-dependence or energy dependence. As a result, it is well adapted only for a small range of nuclear densities, around 1/3 of the normal nuclear matter density.

At intermediate energy, where the interpenetration of the nuclei is important, it is necessary to introduce a density dependence in the interaction. The DDM3Y interaction is defined by [Az85]

$$w(E,\rho,r) = g(E,r)f(E,\rho) \tag{1.21}$$

where

$$f(E,\rho) = C(E)\left[1 + \alpha(E)e^{-\beta(E)\rho}\right] \tag{1.22}$$

and g(E,r) is the original M3Y interaction, whose spin and isospin independent part is given by eq.(1.20). E is the bombarding energy per nucleon, r is the internucleon separation, and ρ is the density of nuclear matter in which the interacting nucleons are embedded. It is usual to assume that the local density is simply the sum of the two individual densities at that point: $\rho(\vec{r}) = \rho_A(\vec{r}_1) + \rho_a(\vec{r}_2)$ for a nucleon at $\vec{r}_1$ in nucleus A interacting with a nucleon at $\vec{r}_a$ in nucleus α. This is called the frozen density approximation. This assumption ignores any readjustments due to their mutual interaction or to the Pauli principle, and is really justified only for peripheral collisions where the density overlap is not large.

The parameters of the density-dependent factor (1.22) were determined at each energy E so that the volume integral w(E,ρ,r) matched the volume integral $V_0(\rho,E)/\rho$ (see fig.1.3) of the real part of the reaction-matrix interaction calculated in the JLM formalism, for various densities of nuclear matter from ρ=0.008 to ρ=0.185 fm^{-3}. Since the parameters of the DDM3Y interaction were fitted to the JLM results, the DDM3Y potential is very close to the JLM one. The parameter values for the energy range E=3 to 90 MeV are shown in Fig.1.8,

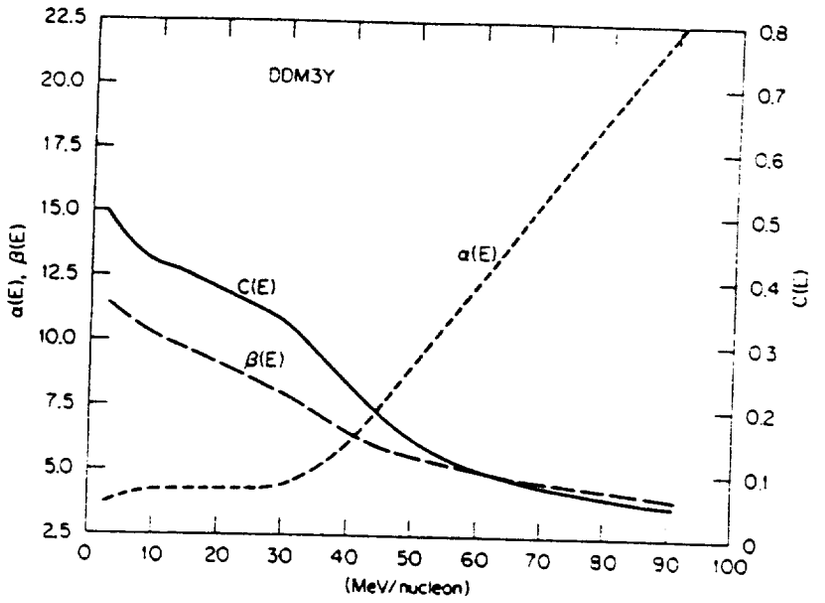

Fig.1.8 Parameter values for the density-dependent factor of eq.(1.22) as functions of the energy per nucleon. The parameters α and C are dimensionless, while β is in units of fm^3.

Because the dependence on density weakens the interaction as the density increases, the potentials obtained by using DDM3Y interaction are much more shallow at small radii, by almost a factor of two. This feature is essential for high energy light ion scattering, which is sensitive to the interior region. Heavy ion elastic scattering is mostly sensitive to the potential in the surface, where the DDM3Y potentials have a slightly less steep slope than the M3Y ones. If the potentials are represented in the vicinity of the strong absorption radii by exponentials $V_0 \exp(-r/\alpha)$, the values α for the DDM3Y are about 10% larger than for the M3Y interaction.

Although M3Y double folded potentials were developed by Satchler to reproduce elastic scattering data below 20 MeV/nucleon, these potentials were also applied at higher energy for different systems [Ro88], [Az85]. The results are illustrated on Fig.1.9-1.11 which present the experimental and calculated angular distributions for the systems $^{16}O+^{12}C$, ^{28}Si, ^{40}Ca, ^{90}Zr and ^{208}Pb at 94 MeV/nucleon.

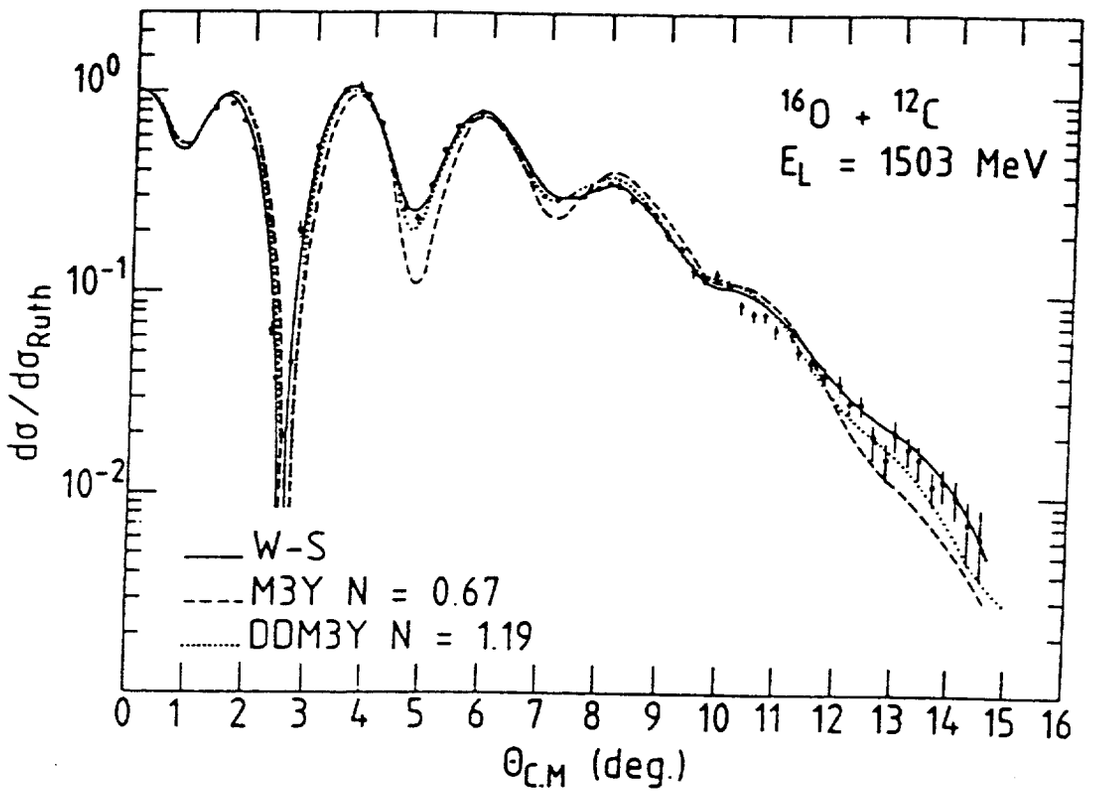

Fig.1.9 Elastic scattering angular distribution measured for the system $^{16}O-^{12}C$ at 94 MeV nucleon.

In each case, the different curves correspond to fits obtained with (W-S) potentials (solid lines), M3Y double folded potentials (dashed lines), or density-

dependent M3Y (DDM3Y) potentials (dotted lines). The imaginary part was assumed to have a Woods-Saxon or in some cases a squared Woods-Saxon form [Ro88]. Indeed, one of the limitations of the double-folded potentials, for heavy ions collisions, is related to the imaginary part of the potential. Even if the nucleon-nucleon interaction is complex, the imaginary part that is deduced by applying the folding procedure is not appropriate for composite systems where additional sources of absorption, such as transfers or break-up, contribute to the imaginary potential and cannot be accounted for by this procedure. Therefore, the imaginary potential has to be treated phenomenologically. The simplest prescription is to assume that it has the same shape as the real folded potential and thus introduce an additional free parameter, the imaginary strength. But it happens that the experimental data require a different shape for the absorptive potential. In these cases a Wood-Saxon potential with 3 free parameters is usually taken. In all cases, very good fits could be obtained, with the exception of the M3Y potential for the lightest targets. The different curves for the three heavy targets could not be distinguished. However these fits correspond to normalization factors which differ considerably from 1. Table 1 gives the values of the normalization factors which were obtained in the fitting procedure. For M3Y potentials, the normalization factor is roughly constant for all systems and equal to 0.66 on average.

These results are summarized in Fig.1.12, with some other results at lower energies or for other systems [Az85], [Br82], [St79], [Sa84], [Br86].

System	$^{16}O+^{12}C$	$^{16}O+^{28}Si$	$^{16}O+^{40}Ca$	$^{16}O+^{90}Zr$	$^{16}O+^{208}Pb$
N(M3Y)	0.67	0.64	0.68	0.64	0.64
N(DDM3Y)	1.19	1.05	1.05	0.87	0.83

Table 1: Normalization factors of double folded potentials which best fit the measured elastic angular distributions, measured at 94 MeV/nucleon.

They show a contrast to the low energy situation where N is roughly equal or even larger than 1. The large values of normalization factor obtained at low energy in the case of the system $^{16}O+^{208}Pb$ are related to the threshold anomaly at the Coulomb barrier. The general trend is a regular decrease from N=1.1 below 20 MeV/nucleon down to 0.7 around 100 MeV/nucleon. This shows that the energy dependence included

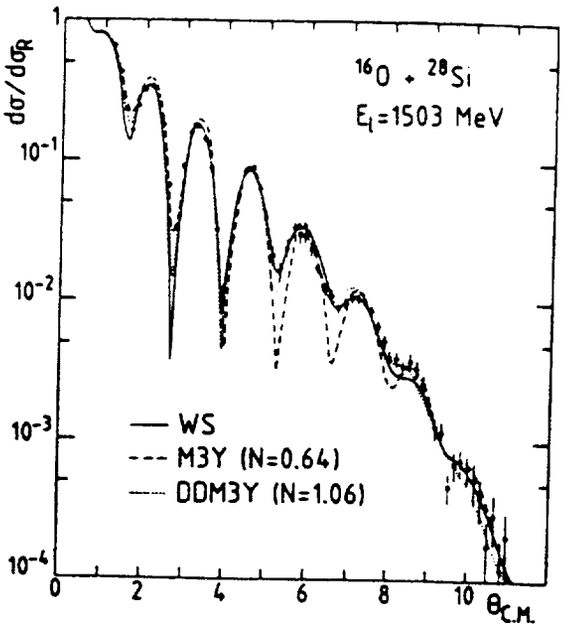

Fig.1.10 Elastic scattering angular distribution measured for the system $^{16}O+^{28}Si$ at 94 MeV/nucleon

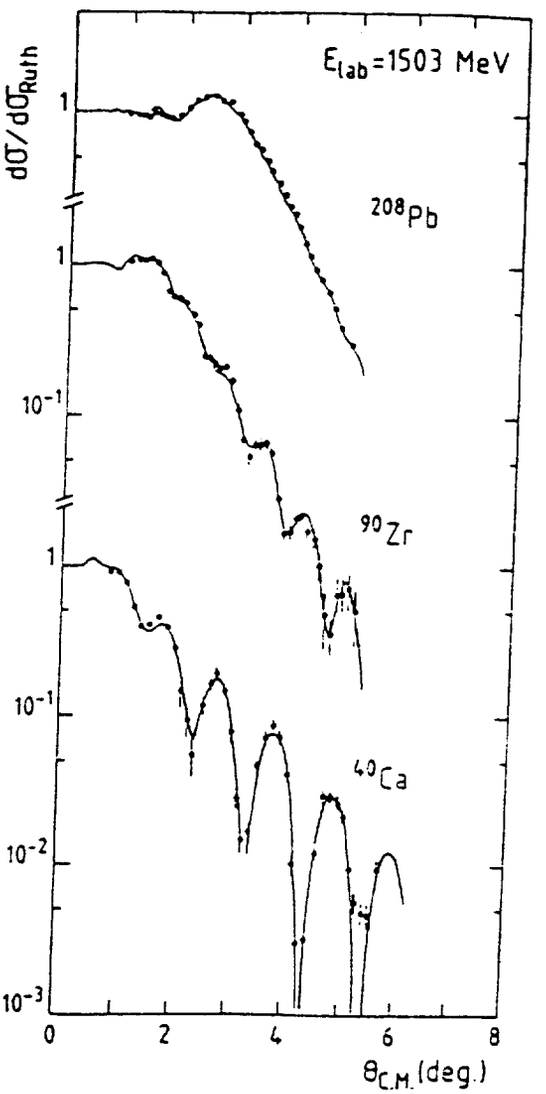

Fig.1.11 Elastic scattering angular distributions measured for the systems $^{16}O+^{40}Ca$, ^{90}Zr and ^{208}Pb at 94 MeV/nucleon

in the M3Y interaction, represented by relation (1.20), is not sufficient to reproduce the real potential reduction at high energy. It is also interesting to note that such an energy dependence is in disagreement with the predictions of microscopic models [Br75], [Br77], [Fa84], [Sa83b], for the nucleus-nucleus potential which predict that, due to the disappearance of Pauli blocking at high energy, the depth of the nuclear potential should increase up to around 50 MeV/nucleon. This discrepancy is, as yet not well understood. However it should be noted that the nucleon-nucleon interaction potential decreases with increasing energy between 10 and 140 MeV [Je77].

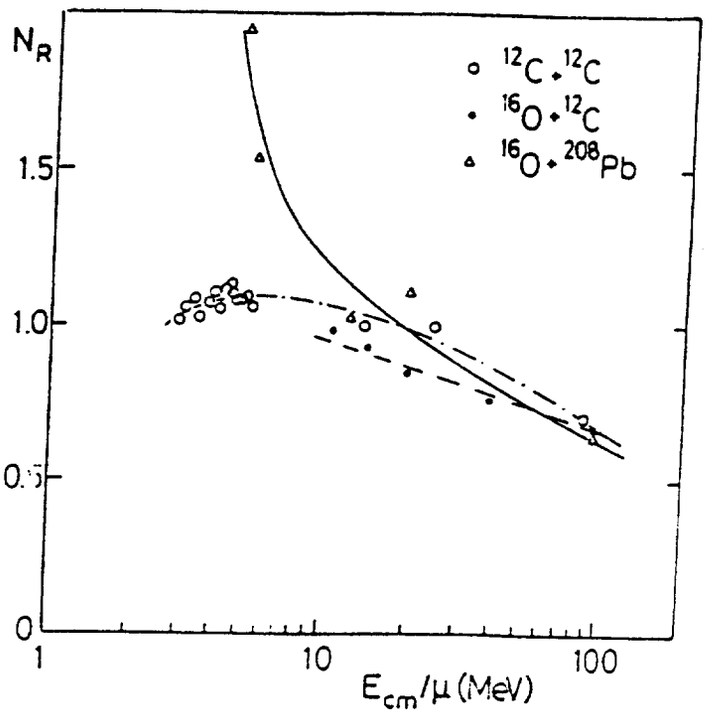

Fig.1.12 Normalization factors of the density independent double folded potentials which best fit the $^{12}C-^{12}C$, $^{16}O-^{12}C$, $^{16}O-^{208}Pb$, and $^{40}Ar-^{60}Ni$, ^{120}Sn, ^{208}Pb elastic angular distributions. The curves are to guide the eye, [Ro88].

Concerning the DDM3Y interaction, the normalization factors obtained decrease from 1.2 for the lightest systems down to 0.8 for the heaviest one. The values deduced for $^{16}O+^{12}C$ and $^{16}O+^{28}Si$ are not very different from those obtained in the case of α elastic scattering (N=1.3) [Ko84], or for the system $^{12}C+^{12}C$ in the same energy range [Br88], whereas the value 0.8 obtained for the heaviest systems is very close to the results found for other heavy systems ($^{40}Ar+^{60}Ni$, ^{120}Sn, ^{208}Pb) or at lower energies

[AZ85]. Therefore one can conclude that the density and energy dependence included in the DDM3Y interaction does not provide an overall description of all data.

These problems are probably related to the fact that both M3Y and DDM3Y interactions cannot reproduce correctly the basic features of normal nuclear matter. For example as mentioned above, the M3Y interaction is well adapted only for a small range of nuclear matter densities at around one third of that of normal nuclear matter.

The total nuclear matter energy per particle is given by,

$$\frac{E}{A} = \frac{3\hbar^2 k_F^2}{10m} + \frac{\rho}{2}\left(J_D + \int\left[\hat{j}_1(k_F r)\right]^2 u_{EX}(r) d^3 r\right) \tag{1.23}$$

where $J_D = \int u_D(r) d^3 r$ is the volume integral of the direct part of the M3Y interaction and $\hat{j}_1(x) = 3j_1(x)/x$ where $j_n(x)$, is the nth order spherical Bessel function. $u_D(r)$ is given by eq.(1.18) and (1.19) whereas $u_{EX}(r)$ is the exchange part of the M3Y interaction evaluated recently by D.T. Khoa et al. [Kh88]. $u_D(r)$ and $u_{EX}(r)$ have the following explicit form:

$$u_D(r) = \left[7999\frac{e^{-4r}}{4r} - 2134\frac{e^{-2.5r}}{2.5r}\right]$$

$$u_{EX}(r) = \left[4631\frac{e^{-4r}}{4r} - 1787\frac{e^{-2.5r}}{2.5r} - 7.847\frac{e^{-0.7072r}}{0.7072r}\right] \tag{1.24}$$

The equilibrium density of the nuclear matter ρ_0 is determined from the saturation condition

$$\frac{\partial}{\partial\rho}\left(\frac{E}{A}\right)\Big|_{\rho=\rho_0} = 0 \tag{1.25}$$

The nuclear compressibility k, is defined as the curvature of the binding energy E/A with respect to the density

$$k = 9\rho^2 \frac{\partial^2}{\partial \rho^2}\left(\frac{E}{A}\right)\Big|_{\rho=\rho_0} \qquad (1.26)$$

Due to the attractive character of the M3Y forces (1.24), the potential-energy term in eq.(1.23) becomes dominant at high densities, and keeps the nuclear matter binding energy decreasing with increasing density (the dash-dotted line in the upper part of Fig.1.13). The saturation condition is therefore not fulfilled and the nuclear matter is collapsing [Kh93]. For the more general expression of the DDM3Y interaction where the exchange potential is properly taken into account,

$$u_{D(EX)}(\rho, r) = f(\rho) u_{D(EX)}(r) \qquad (1.27)$$

where f(ρ) is given by eq.(1.22). With parameters fixed for the low incident energy of 5 MeV/nucleon, the saturation condition (1.25) is fulfilled with the equilibrium binding energy E/A=15.9 MeV and density ρ_0=0.07 fm^{-3} (the dashed line in the upper part of Fig.1.13). The compressibility obtained in this case is K=129.2 fm and corresponds to a very soft equation of state.

D.T. Khoa and W. von Oertzen [Kh93] have readjusted the parameters in eq.(1.22) to reproduce the empirical values of the saturation binding energy (E/A=16 MeV) and density (ρ_0=0.17 fm^{-3}) via eq. (1.25) and (1.26), respectively. The density dependent interaction obtained in this way (DDM3Y1) gives K=149.5 which is close to the lower limit of the compressibility found from different studies of the monopole vibrations (§3-4). The DDM3Y1 parameters are given in table 2 and the nuclear equation of state obtained with this interaction is shown as solid line in the upper part of Fig.1.13. Due to the exponential form of the density dependence in eq.(1.22) one cannot get a higher value for K by readjusting the parameters. To obtain higher values of K, D.T. Khoa and W. von Oertzen [Kh93] chose a different form for f(ρ), which was introduced first by Myers in the single folding calculation [My73]

$$f(\rho) = C(1 - \alpha\rho^{\beta}) \qquad (1.28)$$

The parameters of the new density dependent interactions, dubbed as BDM3Y0 for β=2/3, which is the value originally used by Myers, and BDM3Y1, BDM3Y2 and

BDM3Y3 for integer values of β ranging from 1 to 3, are also given in table 2. Different nuclear equations of state obtained with these interactions are shown in the lower part of (Fig.1.13). One can see that the larger the β parameters the harder the nuclear equation of state.

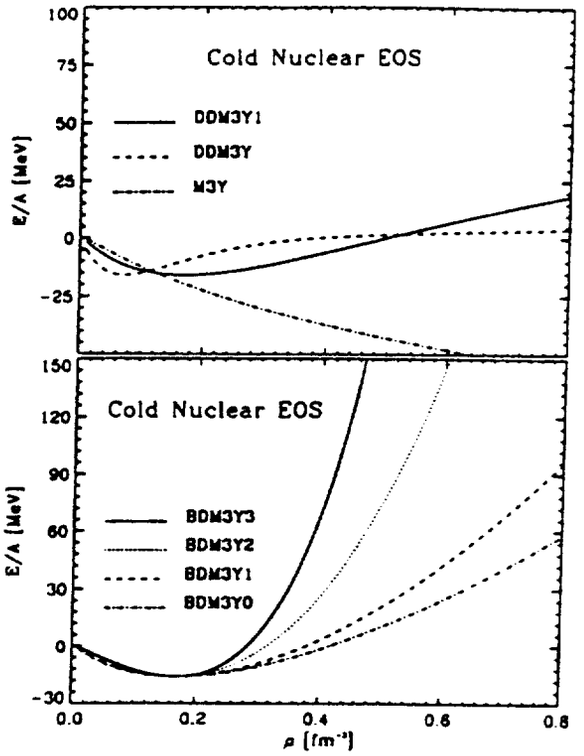

Fig.1.13 Different nuclear equations of state generated by the original M3Y interaction and its DDM3Y, eq.(1.22), density dependent versions (upper part). The lower part shows the results obtained with the BDM3Y, eq.(1.28), density dependence with parameters giving nuclear compressibilities $K \approx 170 \rightarrow 454$ *MeV (table 1), [Kh93].*

It was found that in order to reproduce the energy dependence of the nucleon optical potential, the linear energy dependence (g(E)=1-0.003E) is the most appropriate mathematical expression. The most general form of the energy and density dependent M3Y potential is given by

$$u_{D(EY)}(\rho, E, r) = f(\rho)g(E)u_{D(EY)}(r) \qquad (1.29)$$

where the parameters for f(ρ) are given in table 2.

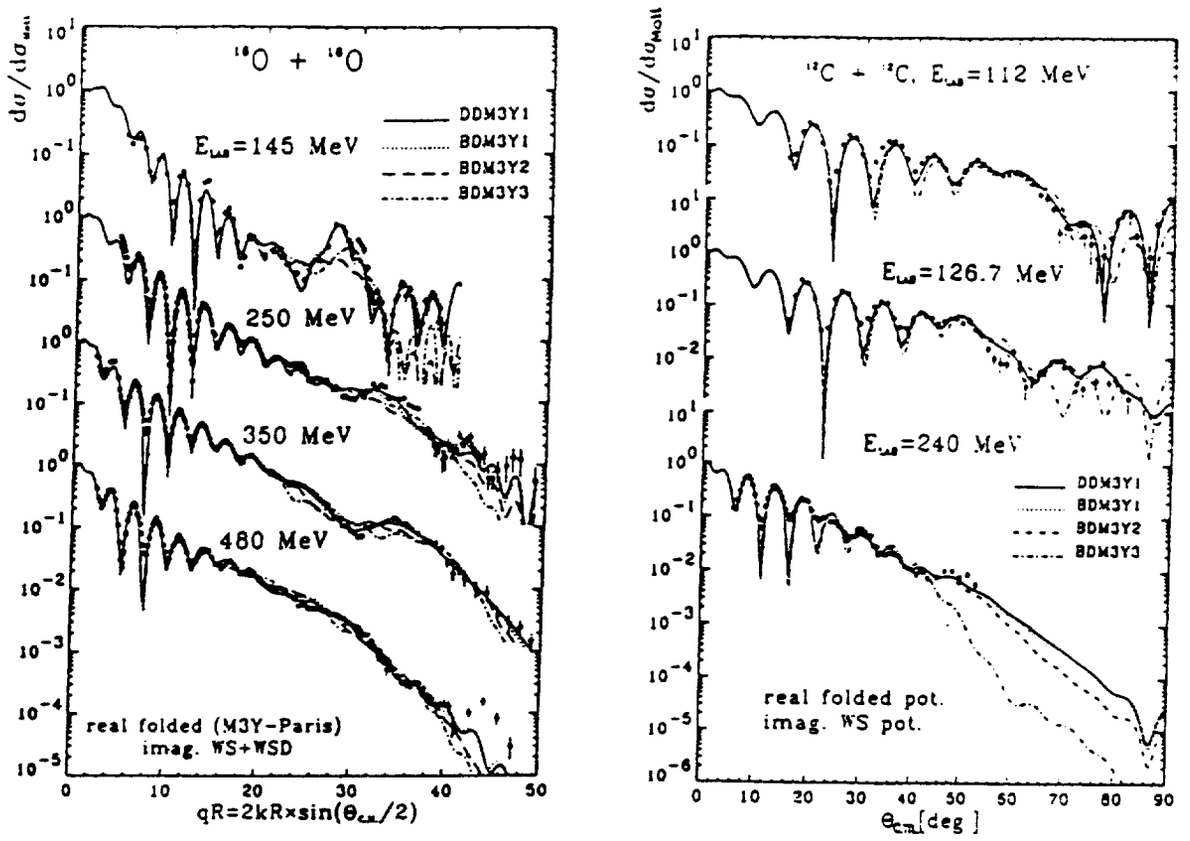

Fig.1.14 Fits of the elastic ^{12}C-^{12}C and ^{16}O-^{16}O scattering data given by different types of the optical potential. The real parts of the optical potential were calculated using different density dependent versions of the M3Y interaction, while the imaginary parts were assumed to have a volume Woods-Saxon shape.

The results obtained with these interactions in the case of light systems such as ^{12}C+^{12}C and ^{16}O+^{16}O between 10 and 30 MeV/nucleon are very impressive [Kh93], [Kh94], [Kh95]. As can be seen in Fig.1.14, very good fits can be obtained on the complete angular range covered by the ^{12}C+^{12}C and ^{16}O+^{16}O data, with a renormalization of the folded potential by at most 10%. Excellent fits were obtained also for the ^{16}O+^{12}C and ^{16}O+^{28}Si data which were measured at somewhat higher energies,

Interaction	f(ρ)	C	α	β	k(MeV)
DDM3Y1	eq.(1.24)	0.2845	3.6391	2.9605 fm^3	149.5
BDM3Y0	eq.(1.30)	1.3827	1.1135 fm^2	2/3	170.1
BDM3Y1	eq.(1.30)	1.2253	1.5124 fm^3	1.0	210.6
BDM3Y2	eq.(1.30)	1.0678	5.1069 fm^6	2.0	332.1
BDM3Y3	eq.(1.30)	1.0153	21.073 fm^9	3.0	453.6

Table 2: Parameters of different dependent versions, eq.(1.22) and eq.(1.28), of the M3Y interaction. The nuclear matter compressibility K was obtained using eq.(1.26).

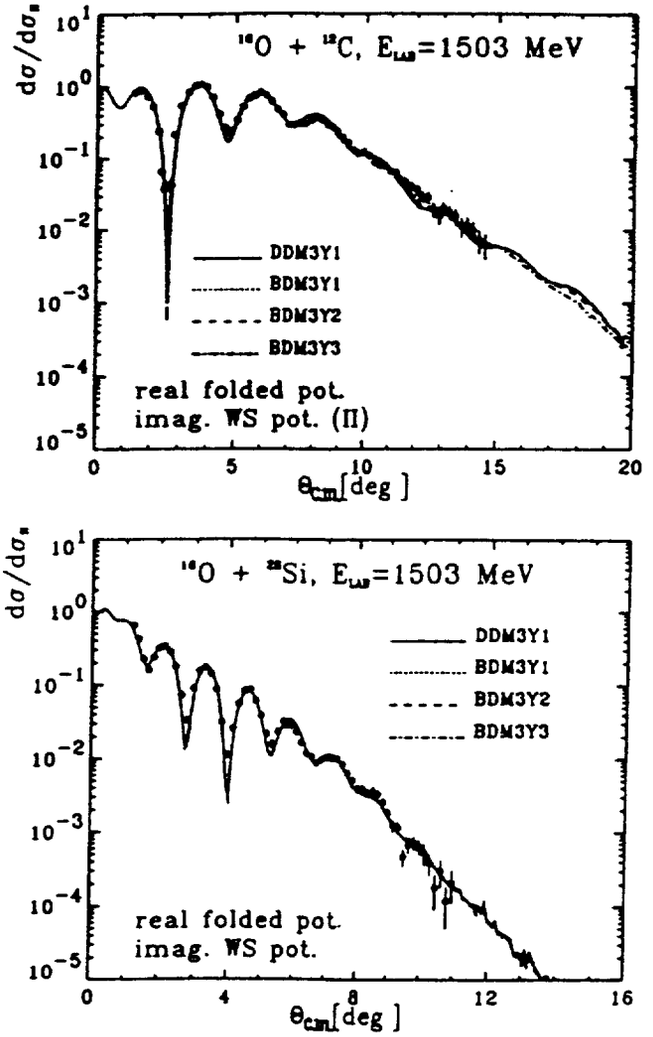

Fig.1.15 The same as Fig.1.14. for the ^{16}O-^{12}C and ^{16}O-^{28}Si data at E_{lab} = 1503 MeV.

(Fig.1.15), [Ro88]. The ^{16}O+^{12}C data at 1503 MeV, have been shown to be sensitive to the real part of the optical potential at distances of 3-6 fm while the « strong absorption » radius for this system is at about 6.2 fm, [Ko88], [Ro85].

The different curves correspond to different parametrisations of the density dependence which generate different equations of state for the cold nuclear matter. In this context, the nuclear density overlap, which occurs during refractive heavy-ion scattering, opens an alternative approach to the study of the equation of state. Indeed, it has been shown that refractive scattering data, which in most cases require a rather transparent optical potential, are very sensitive to the real part of the potential at small distances. Such data imply that among the different types of folded potential, the DDM3Y1 and the BDM3Y1 potentials with parameters given in table 2, are the most relevant ones. From these analyses it was concluded that the nuclear compressibility $K \approx 150 - 210$ MeV is the most realistic for the cold nuclear matter [Kh95].

1-3-b) A new simple effective interaction for peripheral heavy-ion collisions at intermediate energies

The M3Y interaction and its density dependent versions give the real part of the optical potential. The imaginary part in most of the folding analyses, is taken in some phenomenological form with parameters adjusted to give the best fit to the scattering data. In order to overcome this problem, R. Satchler decided to explore a purely phenomenological approach [Sa94], taking a three parameter Yukawa nucleon-nucleon interaction including a real and imaginary part, but assumed to be isoscalar, independent of spin and without any density dependence in a first attempt. It may be written as:

$$v_{NN} = -(v + iw)\frac{e^{-s/t}}{s/t} \qquad (1.30)$$

where s is the distance between the two nucleons. Very good fits were obtained for a large number of data sets, selected between 10 and 100 MeV/nucleon. Fits to the data were optimized by adjusting the values of v and w for a given range of t. Fig.(1.16) shows an example of the quality of the fits and the sensitivity to variations in t when the presence of nearside-farside interference oscillations allows the optimum range to be determined easily. The optimum values determined in this way clustered within $t \approx 0.7 \pm 0.1$ fm, with no indication of a dependence on bombarding energy. This value of t results in fits to the data (with two adjustable parameters v and w) as good as those

obtained with four or more parameters when using a phenomenological Woods-Saxon potential.

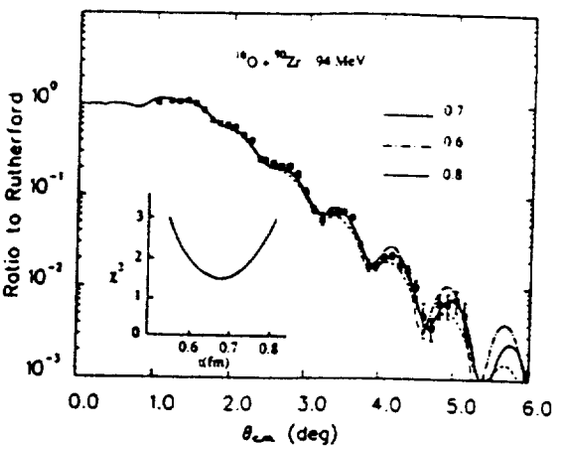

Fig.1.16 Illustrating the sensitivity of the scattering of $^{16}O-^{90}Zr$ at E=94 MeV/nucleon to the range t of the interaction. Solid curve: t=0.7 fm; dash-dotted curve: t=0.8 fm; dotted curve: t=0.6 fm. Inset is showing the variation of χ^2 per datum with range [Sa94]. The data are from Ref. [Ro88].

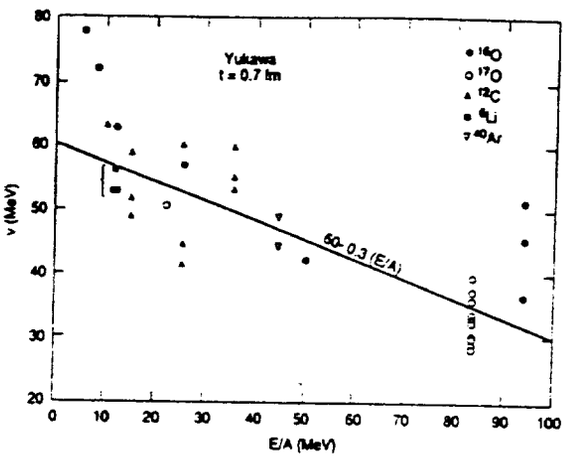

Fig.1.17 Real strengths υ versus energy for various projectile-target combinations, when the range is t=0.7 fm. The projectile is identified by the symbol. The bracket draws the attention to the four data for ^6Li, three of which coincide in value.

There is an apparent discrepancy between the results for ^{17}O on 10 targets at the nearby E=84 MeV/nucleon ($\upsilon \approx 33 \pm 4$ MeV) and those for ^{16}O at E=94 MeV/nucleon ($\upsilon \approx 45 \pm 6$ MeV, see also §1-3-d). If one gives most weight to the ^{17}O data, the energy dependence of the real strength is given qualitatively by the straight line shown in (Fig.1.17) and eq.1.31. The imaginary strength w remains close to the real one; $\upsilon \approx w$ to within about 20%.

$$\upsilon \approx w \approx 60 - 0.3\frac{E}{A}\ \text{MeV} \qquad (1.31)$$

Signs of the threshold anomaly appear for ^{16}O at the lowest energies; υ begins to increase faster than (1.31) when E/A falls below about 10 or 15 MeV/nucleon.

These results will have to be refined in order to introduce, for example, a density dependence which can also reproduce the data presenting refractive features. This interaction is useful as it provides a direct and consistent way of relating the scattering measurements to the underlying nuclear structure, namely, density distributions in the case of elastic scattering and transition density distributions in the case of inelastic scattering.

1-3-c) Isospin and spin dependence of the effective nucleon-nucleon interaction

In general only the isoscalar or central term of the nucleon-nucleon interaction υ_{00} is considered in calculating folded potentials, [eq.(1.2)]. The nucleon-nucleon interaction however depends on isospin [eq.(1.3)]. The isovector term υ_{01} gives a symmetry potential contribution to the folding integral which depends on the difference $(\rho_n-\rho_p)$ between the neutron and proton densities. This latter term vanishes if either or both of the nuclei has zero isospin (or $\rho_n=\rho_p$). It takes the general expression

$$U_\tau(\vec{r}_a) = \iint \left[\rho_{An}(\vec{r}_1) - \rho_{Ap}(\vec{r}_1)\right]\left[\rho_{an}(\vec{r}_2) - \rho_{ap}(\vec{r}_2)\right]\upsilon_{01}(\vec{r}_{12})\,d\vec{r}_1 d\vec{r}_2 \quad (1.32)$$

With the assumption that $\rho_n=(N/Z)\rho_p=(N/A)\rho$, this becomes

$$U_\tau(\vec{r}_a) = \left(\frac{N_a - Z_a}{A_a}\right)\left(\frac{N_A - Z_A}{A_A}\right)\iint \rho_A(\vec{r}_1)\rho_a(\vec{r}_2)\upsilon_{01}(\vec{r}_{12})\,d\vec{r}_1 d\vec{r}_2 \quad (1.33)$$

In the case of the M3Y interaction (eq. (1.18) and (1.19)) $\frac{\upsilon_{01}}{\upsilon_{00}} \approx -0.5$ and therefore one obtains

$$\frac{U_\tau(\vec{r}_a)}{U(\vec{r}_a)} \approx -\frac{1}{2}\frac{N_a - Z_a}{A_a}\frac{N_A - Z_A}{A_A} \qquad (1.34)$$

The influence on the elastic scattering of the isospin part of the nucleon-nucleon potential was investigated recently by J.A. Christley et al. [Ch95b], and even in the case of exotic nuclei such as $^{24}O+^{48}Ca$, causes only minor changes to the elastic scattering distribution.

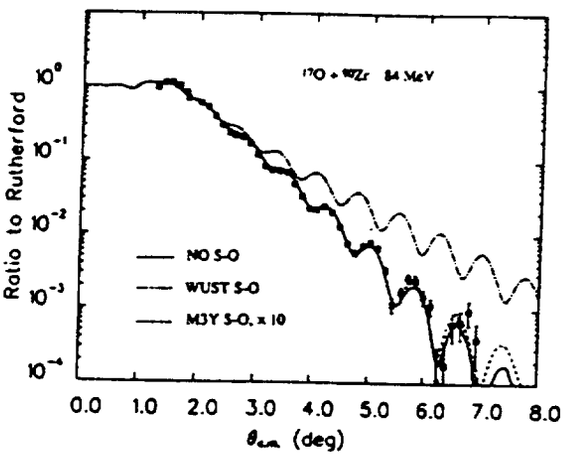

Fig. 1.18 Effects of adding a vector spin-orbit coupling term to the scattering of $^{17}O+^{90}Zr$ at E/A=84 MeV/nucleon. Solid curve: no spin-orbit; dotted curve: addition of spin-orbit term based on M3Y model, with the strength increased ten times; dash-dotted curve: addition of Wust-type spin-orbit term. The data are from [Li93].

The central part of the nucleon-nucleon interaction contains also a spin-spin term. Measurements of the scattering of polarized ^{6}Li ions at the lower energies has demonstrated the presence of spin-orbit coupling, but the effect on the cross section is in general very weak and does not affect heavy-ion elastic scattering results. This contribution was studied for $^{17}O+^{90}Zr$ elastic scattering at 84 MeV/nucleon. To gain some idea of the possible effects of a vector spin-orbit coupling upon the ^{17}O elastic scattering, R. Satchler has made some exploratory calculations, [Sa94]. The first choice was to use a Woods-Saxon parametrisation of the spin orbit potential with parameters $V_{s.o}$=1 MeV, $r_{s.o}$=1.1 fm and $\alpha_{s.o}$=0.7 fm. This set of parameters has been used by Wust et al. [Wu79] to explain polarization effects observed in the $^{88}Sr(^{16}O,^{15}N)$ transfer reaction at low incident energy E/A=6 MeV/nucleon. The other choice was suggested by folding calculations for ^{27}Al on some light nuclei using the M3Y spin-orbit interaction. The resulting spin-orbit potential can be represented by a Woods-Saxon

potential with parameters $V_{s.o}$=1.2 MeV, $r_{s.o}$=0.69 fm and $a_{s.o}$=0.57 fm. Fig. 1.18 shows the results of the calculation for ^{17}O scattering on ^{90}Zr. The cross sections obtained using the short-ranged M3Y-based spin orbit coupling cannot be distinguished from those in the absence of spin-orbit effects, in the angular range measured. Indeed the cross section changes remained very small even when the M3Y spin-orbit potential strength is increased by a factor of ten. Fig. 1.18 demonstrates that the Wust et al. choice of spin-orbit coupling produces large changes in the scattering cross sections. This spin orbit coupling is obviously too strong to be accommodated with what is known on high energy heavy ion elastic scattering. However these theoretical calculations drew attention to the possible role at high energy of spin-orbit coupling for nuclei with non zero spins.

1-3-e) Study of elastic scattering induced by light unstable nuclei

Experimental programs for the study of elastic scattering induced by light unstable nuclei have been started at different laboratories.

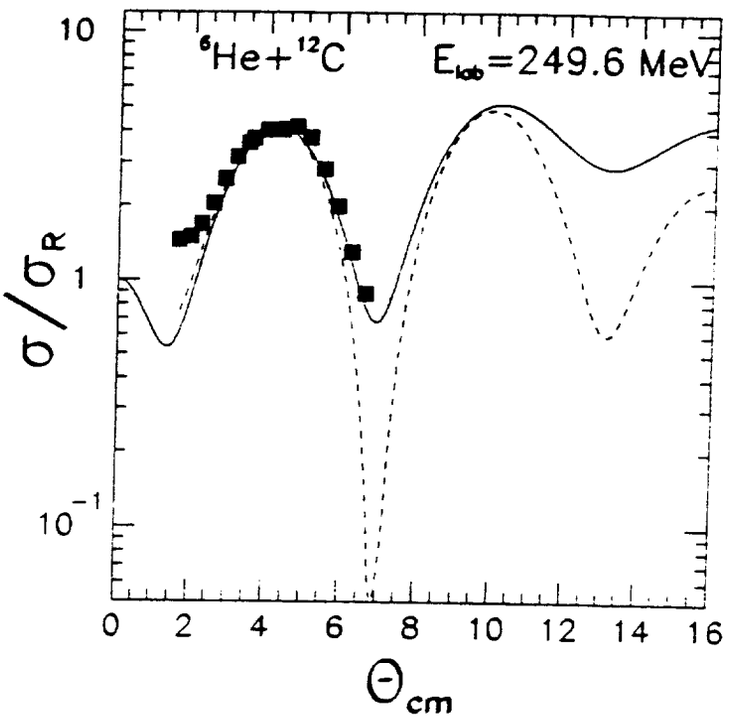

Fig. 1.19 Elastic scattering angular distribution for ^6He-^{12}C at 41.6 MeV u. The solid curve is calculated from the parameter-free four-body eikonal model with a Faddeev wave function for ^6He. The dashed curve was obtained using a density-dependent double folding model.

Measurements of elastic scattering angular distributions of halo nuclei without contaminations from target excitations were obtained recently at GANIL, for the system $^{6}He+^{12}C$ [Kh96]. The theoretical cross section was calculated within a few-body eikonal model. To calculate ^{6}He elastic scattering the model requires three inputs: the ^{6}He three-body wave function plus the $\alpha+^{12}C$ and $n+^{12}C$ optical potentials at the relevant energy per nucleon. Once these are chosen the calculation is completely parameter-free. Fig. 1.19 shows the measured angular distribution plotted against the result of the four-body calculation using a realistic Faddeev model wave function for ^{6}He (solid curve). The dashed curve is the result obtained by folding the ^{6}He density and a 2-parameter Fermi density-dependent DDM3Y interaction. This kind of calculation has been successful in describing elastic scattering of light stable beams on a ^{12}C target in the same energy range, and it is interesting to see how it compares with data with unstable neutron rich beams. The present data do not extent far enough to distinguish unambiguously between the results. The deep minimum in the dotted curve at 7° may be due to ambiguities in the imaginary potential in this kind of calculation. Further experiments extending at backward angles would be of interest to explore this issue.

2. INELASTIC SCATTERING

2-1. THE DISTORTED WAVE BORN APPROXIMATION

The goal here is to present a simplified description of inelastic scattering for collective transitions, since these transitions are particularly sensitive to collective aspects such as the deformation of a nucleus, which can be derived by microscopic calculations. Inelastic scattering experiments provide therefore a testing ground for various theoretical models.

The dynamical theory of the collective motion of a liquid drop is developed in terms of collective oscillations of the surface. The behavior of the surface may be described by the expression:

$$R(\theta,\phi) = R_0\left[1 + \sum_{\lambda\mu} \alpha_{\lambda\mu} Y_\lambda^\mu(\theta,\phi)\right] \tag{2.1}$$

where θ,ϕ are the polar angles with respect to an arbitrary space-fixed axis, and Y_λ^μ is a spherical harmonic of order λ and projection μ. If the drop is incompressible, R_0 is the radius of the undisturbed spherical surface. Collective motion is described by allowing the coefficient $\alpha_{\lambda\mu}$ to vary with time. A $\lambda=1$ deformation corresponds simply to a shift of the center of mass, while $\lambda=0$ involves compression.

In the rotational model it is assumed that the nucleus has a permanent deformation so that, in the case of axial symmetry, the nuclear surface can be defined in the body-fixed system by the expression

$$R(\theta) = R_0\left[1 + \sum_\lambda \beta_\lambda Y_\lambda(\theta)\right] \tag{2.2}$$

since for axial symmetry $\alpha_{\lambda 0} = \beta_\lambda$ and $\alpha_{\lambda\mu\neq 0} = 0$, where β_λ is the usual deformation parameter.

The most frequently used method to analyze inelastic scattering data, is the distorted wave Born approximation (DWBA). In this approximation the transition matrix element for inelastic scattering from the initial state i to a definite final state f can be written as [Ba77]:

$$T_{fi} = \int x_f^{-*}(\vec{k}', \vec{r}) \langle \varphi_f(\xi) | V(\vec{r}, \xi) | \varphi_i(\xi) \rangle x_i^{+}(\vec{k}, \vec{r}) d\vec{r} \tag{2.3}$$

where x_i^+, x_f^- are the solutions for the optical potential with outgoing and incoming boundary conditions respectively, φ_i, φ_f are the initial and final nuclear wave functions and ξ represents all the relevant internal co-ordinates of the target nucleus.

It is convenient to make a multipole expansion of $V(\vec{r}, \xi)$ so that the nuclear matrix element becomes

$$\langle \varphi_f | V | \varphi_i \rangle = \sum_{LM} (I_i M_i LM | I_f M_f) \langle I_f \| V \| I_i \rangle \{ i^L Y_L^M(\vec{r}) \}^* \tag{2.4}$$

The reduced matrix element is a function of r only and is usually written in the form

$$\langle I_f \| V \| I_i \rangle = A_L F_L(r) \tag{2.5}$$

where the magnitude and the form of the factors depend on the nuclear model chosen.

The differential cross section for inelastic excitation is obtained by taking the sum over final states M_f and average over initial states M_i and becomes

$$\frac{d\sigma}{d\Omega} = \left[\frac{\mu}{2\pi\hbar^2} \right]^2 \frac{k'}{k} \sum_{LM} \frac{(2I_f + 1)}{(2I_i + 1)(2L + 1)} |T_{LM}|^2 \tag{2.6}$$

where

$$T_{LM} = i^L A_L \int x_f^{-*}(\vec{k}', \vec{r}) F_L(r) Y_L^{M*}(\vec{r}) x_i^{+}(\vec{k}, \vec{r}) d\vec{r} \tag{2.7}$$

The expression (2.6) for the transition matrix elements has a general and fairly simple form. The characteristic features of the nuclear excitation enter through the reduced matrix elements $A_L F_L(r)$. The macroscopic approach for the description of

these excitations is based on the assumption that the interaction potential $V(\vec{r},\xi)$ follows the deformation of the nuclear surface. A Taylor-series expansion about $R=R_0$, gives

$$V(r-R(\theta,\varphi)) = V(r-R_0) - \delta R\frac{d}{dr}V(r-R_0) + \frac{1}{2}(\delta R)^2\frac{d^2}{dr^2}V(r-R_0)+\ldots \tag{2.8}$$

where θ,ϕ are referred to the body fixed axes. The lowest order term of this expansion can be associated with the usual optical potential, used to describe elastic scattering, while the higher order terms are responsible for inelastic excitation and some corrections to elastic scattering. From equations (2.1),(2.2) and (2.8) and for an excitation from the ground state $I_i=0$ to a final state $I_f=L$ and assuming axial symmetry, the reduced matrix element in the case of the rotational model is given by the expression

$$A_L F_L(r) = \langle I_f = L \| V \| I_i = 0 \rangle = -i^L \beta_L R_0 (2L+1)^{-1/2}\frac{dV}{dr} \tag{2.9}$$

and in the case of the vibrational model by the expression

$$A_L F_L(r) = \langle I_f = L \| V \| I_i = 0 \rangle = -i^L \left(\frac{h\omega_L}{2c_L}\right)^{1/2} R_0 \frac{dV}{dr} \tag{2.10}$$

where $h\omega_L$ is the energy of the phonon and c_L the restoring force parameter.

The form factor of the transition potential is determined from the potential which fits elastic scattering, so that the only free parameters are β_L or $(h\omega_L/2c_L)$. There are no other free parameters. Because of these features, the extended optical model has become the standard method for the analysis of experimental data on inelastic scattering and has been used with great success for a wide range of projectiles, targets and incident energies.

2-2. THE DEFORMATION PARAMETERS

In this description of inelastic scattering, the form factor of the transition potential has a nuclear and a Coulomb part. The nuclear part $F_{L,n}(r)$ is given by the expression (2.9)

$$F_{L,n}(r) = \delta_{L,n} \frac{dV(r)}{dr} \quad [1] \tag{2.11}$$

and the Coulomb part

$$F_{L,c}(r) = \frac{3\delta_{L,c} Z_P Z_T e^2}{2L+1} x \tag{2.12}$$

$$x = R_c^{L-1} / r^{L+1} \quad \text{if } r > R_c$$

$$x = r^{L+1} / R_c^{L+2} \quad \text{if } r < R_c$$

where $\delta_{L,n}$ is the hadronic deformation length related to the nuclear deformation β_n by

$$\delta_{L,n} = \beta_n R_0 \tag{2.13}$$

and $\delta_{L,c}$ is the charge deformation length related to the charge deformation β_c by

$$\delta_{L,c} = \beta_c R_c \tag{2.14}$$

and are obtained from inelastic scattering measurements. In the sharp cut-off limit, the charge deformation is related to the reduced electric transition probability ($B(EL\uparrow)$ by

---

[1] With the notations of the code ECIS of J. Raynal [Ra81]: $F_{L,n}(r) = \frac{\delta_{L,n}}{\sqrt{4\pi}} \frac{dV(r)}{dr}$

$$B(EL\uparrow) = (\frac{3Z_T\beta_c R^L}{4\pi})^2 e^2 fm^{2L} \qquad (2.15)$$

where $R = 1.2A_T^{1/3}$.

The transition probability $B(EL\uparrow)$ can be obtained by many methods such as Coulomb excitation measurements, lifetime measurements or electron scattering. Coulomb excitation and (e,e') measurements are sensitive to the properties of charge deformation. On the contrary, light- and heavy-ion inelastic scattering is sensitive to both the mass and charge deformation in a ratio which depends on the incident energy, the charge product of the colliding nuclei and the multipolarity of the transition.

There is no straightforward way to relate the charge deformation length to the hadronic deformation length and different prescriptions have been used in the past. In some studies the charge deformation is fixed at values taken from Coulomb excitation or (e,e') measurements, while the nuclear deformation is allowed to vary to best describe the data. Most often equality of deformation lengths is assumed, based on the assumption that the neutron and proton distribution are similar and that the two nuclei interact at their mutual edges [He73],

$$\delta_{L,n} = \delta_{L,c} \qquad (2.16)$$

Another source of uncertainty when the projectile is composite, especially a heavy ion, arises from the finite size of the projectile. This ambiguity is also mitigated (but not entirely removed) by assuming that the deformation length is the significant quantity.

2-3. EXAMPLES OF INELASTIC SCATTERING

Excitation of the 2^+ state in ^{208}Pb by ^{17}O+^{208}Pb inelastic scattering

In Fig.2.1 the experimental and calculated angular distribution for the excitation of the 4.09 MeV 2^+ state in ^{208}Pb are presented. The experiment was carried out at GANIL by bombarding a ^{208}Pb target with an ^{17}O beam at E_{lab}=1435 MeV [Li93]. The scattered particles were detected with the high resolution spectrometer SPEG.

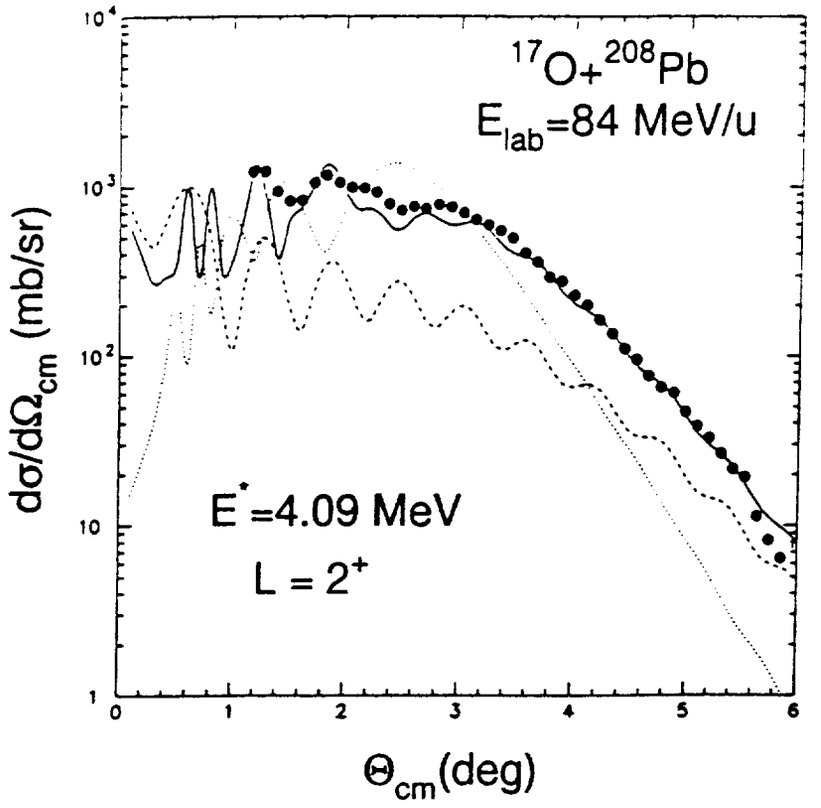

Fig.2.1 Experimental and calculated angular distributions for the 4.09 MeV 2$^-$ state in ^{208}Pb. The solid line is the result of the coupled channel calculation. The dashed and dotted lines show, respectively, the nuclear and Coulomb contributions to the cross section.

The adopted B(E2) value for this state is $B(E2\uparrow) = 0.29 \pm 0.03 e^2b^2$ [Ra89], which leads (2.15) to a Coulomb deformation of 0.054. The nuclear deformation was calculated by applying equation (2.16). The calculated angular distribution is in good agreement with the experimental results. Calculations assuming only Coulomb interaction (dotted lines) and only nuclear interaction (dashed lines) are also plotted. The Coulomb excitation dominates in the angular region 2-4°. Hence this 2$^+$ inelastic scattering is an almost model-independent measurement of the $B(E2\uparrow)$.

Excitation of the 3$^-$ state in ^{208}Pb by ^{17}O+^{208}Pb inelastic scattering

In Fig.2.3 the experimental and calculated angular distribution for the excitation of the 2.61 MeV 3$^-$ state in ^{208}Pb are presented. These results were obtained simultaneously with the 2$^+$ inelastic scattering data presented in Fig.2.1. The calculated

angular distribution has a deep minimum between 2 and 3 degrees. The data lie above the calculation due to the contribution of ^{17}O elastically scattered events on ^{12}C contaminant in the target.

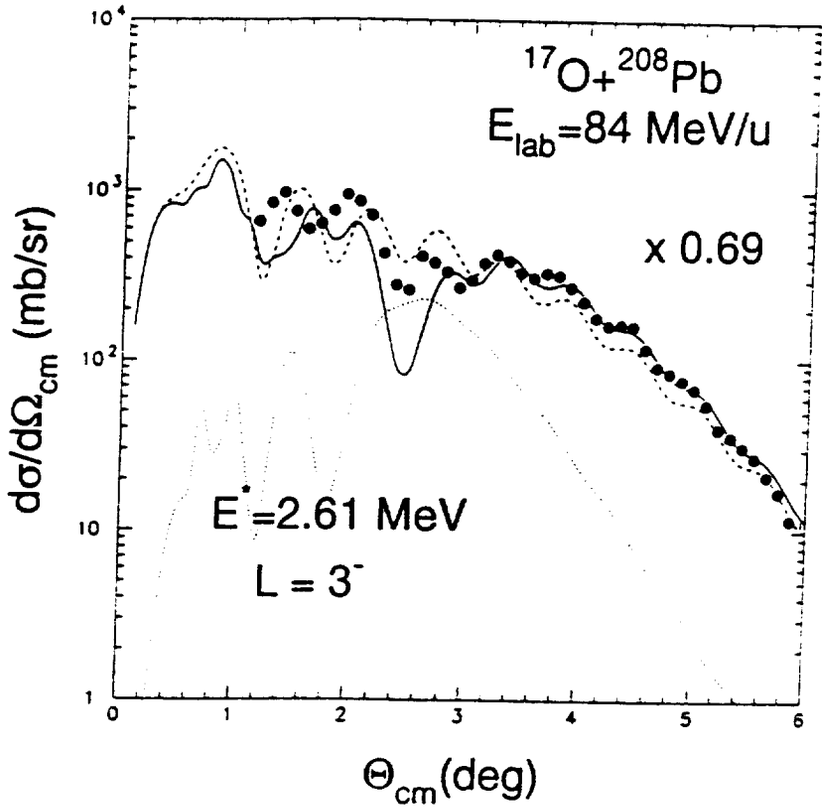

Fig.2.3 Experimental and calculated angular distributions for the 2.61 MeV 3$^-$ state in ^{208}Pb. The solid line is the result of the coupled channel calculation. The dashed and dotted lines show, respectively, the nuclear and Coulomb contributions to the cross section. The B(E3) value resulting from the fit of the data is smaller than the adopted value by 30%.

Calculations assuming only Coulomb (dotted line) and only nuclear interaction (dashed line) are also plotted. Due essentially to the $1/r^{L+1}$ behavior (2.12) of the electromagnetic interaction, the excitation of this state is dominated by the nuclear interaction. The B(E3) value resulting from the fit of the data is smaller than the adopted value by 30% (Table 3). It was concluded that « hindrance » in the excitation of the first 3$^-$ states is observed when the targets ^{208}Pb, ^{120}Sn, ^{60}Ni are studied.

This apparent hindrance was explained recently by R. Satchler and collaborators who have demonstrated that this is a consequence of using the deformed optical model to analyze the hadronic scattering. It disappears when a folding model is used [Be93].

Excitation of the 2^+ state in ^{32}Mg by ^{32}Mg+^{208}Pb inelastic scattering

Assuming that we understand how to calculate inelastic scattering, then we can deduce from inelastic scattering measurements useful spectroscopic information on nuclei, as shown in the following example. The deformation of the very neutron-rich nucleus ^{32}Mg was obtained recently by measuring ^{32}Mg+^{208}Pb inelastic scattering. This experiment was performed at RIKEN. A primary ^{40}Ar beam of 94MeV/u bombarded a production ^{9}Be target. The various products of projectile fragmentation reactions were analyzed by the projectile separator RIPS to obtain a radioactive ^{32}Mg beam.

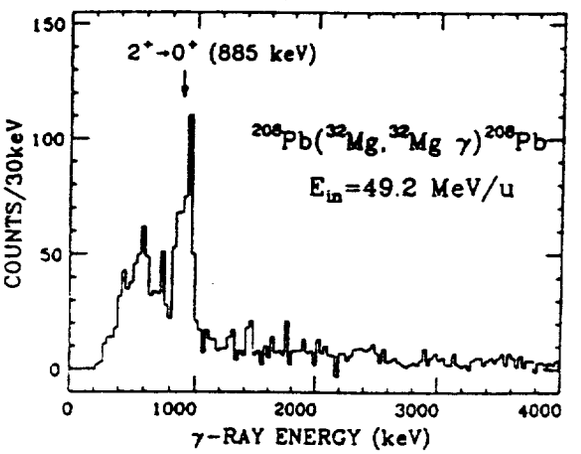

Fig.2.2 Energy spectrum of γ rays emitted from ^{32}Mg-^{208}Pb inelastic scattering at 49.2 MeV u. The Doppler shift is corrected for.

The scattered ^{32}Mg nuclei were detected by a telescope of silicon detectors. The particle identification was achieved by the ΔE-E method and was good enough for the purpose of selecting ^{32}Mg among other Mg isotopes. Sixty NaI(Tl) scintillators surrounded the target to detect the γ-rays. Fig.2.2 shows the γ-ray energy spectrum associated with the ^{32}Mg+^{208}Pb inelastic scattering. The photo-peak at 0.89 MeV corresponding to the $2^+ \rightarrow 0^+$ transition is clearly observed [Mo94].

An experimental deformation parameter $\beta_c = 0.522 \pm 0.04$ was extracted by comparing the experimental cross-section with coupled channel calculations and assuming Coulomb and nuclear deformation parameters equal, $\delta_n = \delta_c$. The measured $B(E2\uparrow) = 0.454 \pm 0.078 e^2 b^2$ is in good agreement with theoretical calculations [Fu92] suggesting a large deformation and vanishing of the N=20 shell gap in ^{32}Mg.

2-4. THE FOLDING MODEL FOR DESCRIBING INELASTIC SCATTERING

Usually, inelastic scattering measurements are analyzed using a deformed optical model potential (DP), as described in § 2.1. This model is often justified by arguing that the potential U follows the shape of the density distribution when the latter is deformed. However a more direct and consistent approach is to obtain the transition potential directly from the transition densities by folding them with an effective nucleon-nucleon interaction and the ground state density of the nucleus which is not excited. This is an obvious extension of the folding model for elastic scattering. For consistency the same folding model should be used for both the diagonal (elastic) and the off-diagonal (coupling) potentials.

Non spherical densities appear now in the folding integral, which can be expanded into multipoles

$$U_F(\vec{r}_\alpha, x_\alpha) = \sum_{l,m} U_{l,m}(r_\alpha, x_\alpha)[i^l Y_l^m(\hat{r}_\alpha)]^* \tag{2.17}$$

whereas the same kind of expansion can be written for these deformed densities

$$\rho(r,\theta,\varphi) = \sum_{l,m} \rho_{l,m}(r)[i^l Y_l^m(\theta,\phi)]^* \tag{2.18}$$

and by inversion

$$\rho_{l,m}(r) = i^l \int \rho(r,\theta,\phi) Y_l^m(\theta,\phi) d\hat{r} \tag{2.19}$$

where

$$d\hat{r} = \sin\theta d\theta d\phi$$

These multipoles play the role of transition densities for inelastic transitions. In the expansion (2.17), the internal coordinates x_α simply stands for the sets of deformation variables $\alpha_{\lambda,\mu}$.

To take a simple case, let us consider a spin-independent effective interaction and only s = t = 0 excitations of the target A, with the projectile α remaining spherical. One can consider that the integration over $\vec{r}_2$ has been done in the folding integral, resulting in an effective interaction $\overline{v}(r_{1\alpha})$ between the projectile and each target nucleon, with $\vec{r}_{1\alpha} = \vec{r}_1 - \vec{r}_\alpha$ (see Fig. 1.1). Then the folding integral (1.2) takes the single-folded form (1.1). Now make a multipole expansion of $\overline{v}(r_{1\alpha})$ about the center of mass of the target A

$$\overline{v}(r_{1\alpha}) = \sum_{lm} \overline{v}_l(r_1, r_\alpha) Y_l^m(\hat{r}_\alpha)^* Y_l^m(\hat{r}_1) \tag{2.20}$$

If we insert this in the folding integral (1.1) and compare with relation (2.19), we obtain an expansion which can be identified with (2.17):

$$U_{lm}(r_\alpha, x_\alpha) = \int \rho_{A,lm}(r_1, x_\alpha) \overline{v}_l(r_1, r_\alpha) r_1^2 dr_1 \tag{2.21}$$

This is not the simplest way to compute U_{lm}, but this expression clearly shows the angular momentum structure, in particular that the 2^l -pole transition selects the corresponding 2^l -pole moment of $\overline{v}(r_{1\alpha})$.

If the density multipole for A is taken to first order only, then

$$\rho^{(1)}_{A,lm}(r) = i^l g_{A,l}(r) \alpha_{lm}(A) \tag{2.22}$$

and the resulting potential multipole has the form

$$U^{(1)}_{lm}(r_\alpha, x_\alpha) = i^l G_{A,l}(r_\alpha) \alpha_{lm}(A) \tag{2.23}$$

where

$$G_{A,l}(r_\alpha) = \int g_{A,l}(r_1) \overline{v}_l(r_1, r_\alpha) r_1^2 dr_1 \tag{2.24}$$

Integral (2.24) is most simply expressed and evaluated in terms of Fourier transform. (for details see [Sa83], Appendix C)

$$G_{A,l}(r) = (2\pi^2)^{-2} \int k^2 j_l(kr) \tilde{\upsilon}(k) \tilde{g}_{A,l}(k) \tilde{\rho}_\alpha(k) dk \qquad (2.25)$$

where $j_l(x)$ is the spherical Bessel function. It remains to specify the transition densities. The most commonly used are, for $l \geq 2$, the Bohr-Mottelson [Bo75] form

$$g_l^{BM}(r) = \delta_l^m \frac{d\rho_A(r)}{dr} \qquad (2.26)$$

and the Tassie form [Ta56]:

$$g_l^T(r) = -\alpha_l^m r^{l-1} \frac{d\rho_A(r)}{dr} \qquad (2.27)$$

where $\rho_A(r)$ is the ground state density of the nucleus being excited, and δ_l^m is the corresponding matter deformation length. We shall only use here the BM form, and we shall assume that the matter and potential surface displacement are equal:

$$\delta_l^U = \delta_l^m \qquad (2.28)$$

From relation (2.24), it clearly appears that the radial form factor G(r) remains dependent on l even if the radial shape of the density multipole is not, except in the limit that $\bar{\upsilon}$ has zero range.

This is a fundamental difference with the standard deformed potential model relation (2.11), which is illustrated on Fig.2.4. This Figure compares the l-independent G_l^{DP} ($F_{L,n}$ in relation 2.11) and the explicitly folded transition potentials (relation 2.24) obtained from the doubled folded optical potential with the complex effective nucleon-nucleon interaction (1.32). All have units deformation lengths ($\delta_l = 1fm$) [Be95]. The various transition potentials have similar shapes, but the magnitudes of the folded ones decrease as the multipolarity increases. These differences illustrate the different results obtained on the one hand by folding over a spherical distribution and deforming the

result, and on the other hand by deforming the density and then folding. "Folding and deforming do not commute" [Be96].

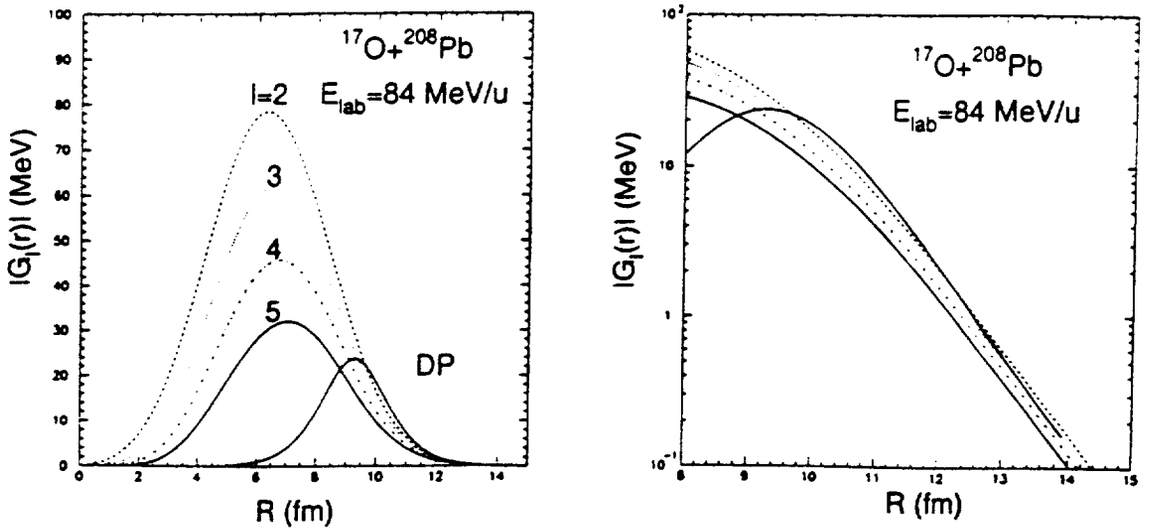

Fig.2.4 Transition potentials for $^{17}O+^{208}Pb$ at E/A=84MeV for deformation lengths of δ_l = 1 fm. i) Left part, curves from the folding model for l=2-5; solid curve (independent of l) from the deformed potential (DP) model. ii) Right part, logarithmic plot of the potentials in the surface region to which the scattering is sensitive.

As the inelastic cross sections are proportional to the square of the transition potentials in the region of the strong absorption radius which is about 11 fm for the system $^{17}O+^{208}Pb$, it is clear that the cross section predicted for a given deformation length by the folding model are smaller than those predicted by the deformed potential optical model and that this difference increases with the multipolarity. For instance, the difference between the cross sections estimated within the deformed potential optical model and the folding model σ^{DP} / σ^{F} reaches the value 78 for l=8 in the case of the ^{90}Zr target. This effect is already very important for octupole transitions. It had been reported in several papers [Sp89], [Ho90], [Ho91],[Li93] where the data had been analyzed within the deformed potential model that the octupole states excited hadronically by light and heavy ions are frequently weaker than what would be expected from electromagnetic measurements.

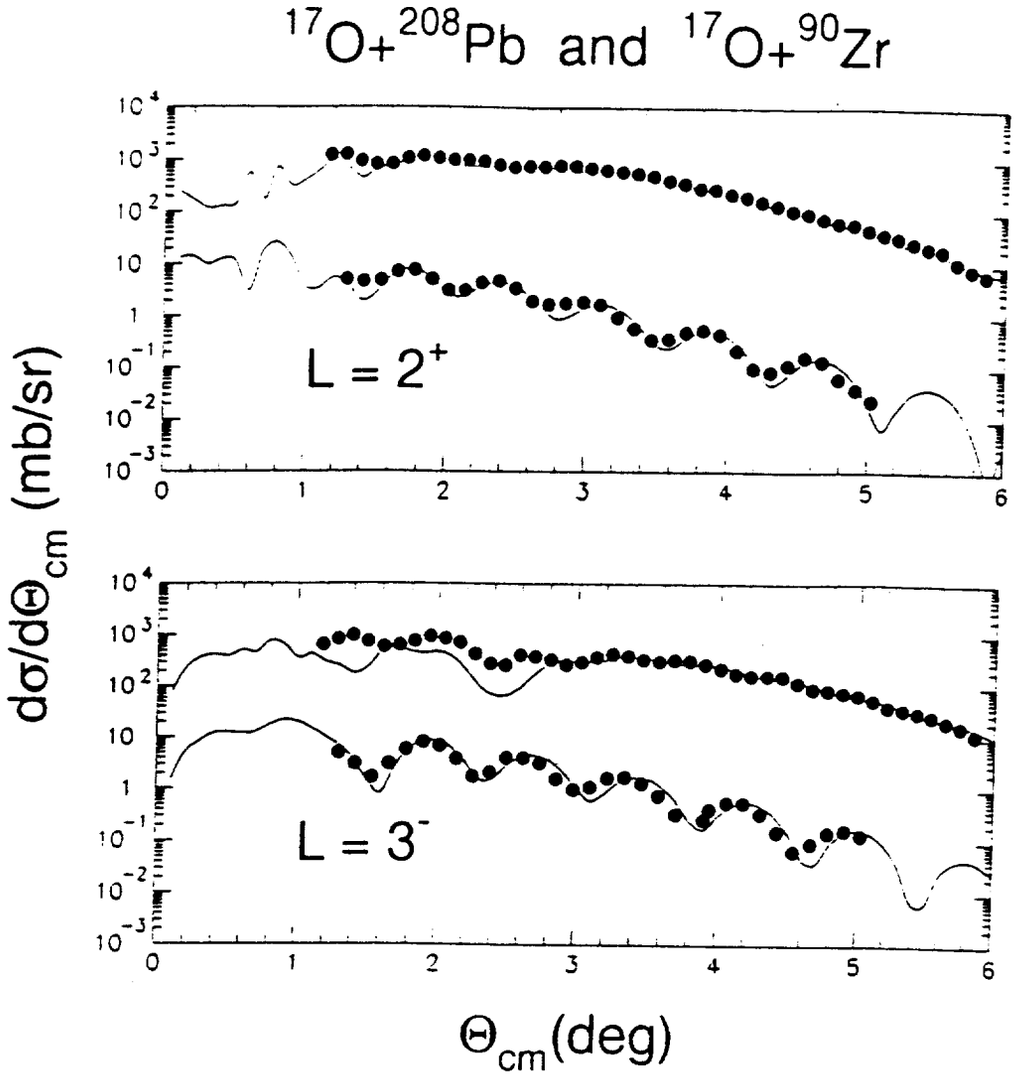

Fig.2.5 Comparison of the theoretical differential cross sections with the measured ones [Li93] for $^{17}O-^{208}Pb$ and $^{17}O-^{90}Zr$ at E/A=84MeV. The B(EL) values used to calculate these curves are compatible with the adopted ones.

Table 3, show the B(E3) values obtained from measurements of ^{17}O inelastic scattering at 84MeV/u on ^{60}Ni, ^{90}Zr, ^{120}Sn and ^{208}Pb. The inelastic scattering angular distributions were analyzed within the deformed potential model. The discrepancy between the reduced transition probability, B(E3), deduced from these measurements within a deformed potential model, $B(E3)_{exp}$, and the adopted values, $B(E3)_{adop}$, reaches a factor between 2 and 4.

However a reanalysis of these data within the folding model using again the complex effective nucleon-nucleon interaction (relation 1.32) and Fig.2.5 showed that the apparent hindrance was removed when the folding was used [Be95]. The excitation

of the 2^+ states for the same targets was not affected because it was dominated by the Coulomb excitation and therefore did not depend on the treatment of the nuclear excitation. On the opposite, the effect becomes dramatic as the multipolarity increases.

Target	^{60}Ni	^{90}Zr	^{120}Sn	^{208}Pb
$B(E3)_{exp}$ (e^2b^L)	0.010 ± 0.002	0.027 ± 0.005	0.075 ± 0.008	0.42 ± 0.04
$B(E3)_{adop}$(e^2b^L)	0.0208	0.108	0.115	0.611

Table 3: Reduced transition probabilities for the excitation of the 3^- low-lying states

The difference between the results obtained from the two models can be traced to the finite range of the effective interaction used when folding. The deformed potential model can be consistent with the folding model only in the limit of zero range [Be93]. This effect of finite range on the transition potential is strongly dependent on the multipolarity l, and can become very large for larger l values. It is therefore recommended to use a folding model to extract deformation lengths and multipole moments from inelastic scattering measurements.

3. ELECTRIC GIANT RESONANCES

This chapter will be devoted to electric giant resonances. Most of the necessary theoretical background information can be found in the books of Bohr and Mottelson [Bo75] and R. Satchler [Sa83]. Several review papers have appeared which cover the state of the field on giant resonance studies [Be81],[Sp81],[Wo87]. The most recent is the review on electric and magnetic giant resonances in nuclei, edited by J. Speth [Sp91], in which the reader can find an important amount of information. The recent developments concerning multiphonon excitations can be found in the review article of Ph. Chomaz and N. Frascaria [Ch95].

3-1. PHENOMENOLOGY

The occurrence of collective modes is a common feature of quantum many-body systems. They have greatly contributed to our understanding of the bulk behavior of such systems and their non equilibrium properties. Among the elementary modes of nuclear collective motion various types of giant resonances are now well established. Giant resonances are defined as resonance structures in the transition strength distribution of an external field which carry a large fraction of the total transition strength (typically of the order of 50% or more). They occur in the whole periodic table and their characteristic parameters, like energy, width, decay probabilities etc. are smooth functions of the mass number A.

The first Giant Resonance which was observed in nuclei in 1947 is the Isovector Giant Dipole Resonance (GDR). The study of this mode became possible after the invention of the Betatron which made available high energy γ-ray beams. A photon carries with it an oscillating electric field of a wavelength larger than the diameter of a nucleus. As a result the electric field associated with a passing γ-ray is nearly uniform across the nucleus. The field exerts a force on the positively charged protons, moving them away from neutrons. The neutrons themselves are electrically neutral, and so the field has no direct influence on them. Because the center of mass of the nucleus remains at rest, however, the neutrons move in the opposite direction. The proton and neutron oscillations are opposite to each other and the mode is called isovector ($\Delta T=1$). The restoring force of the vibration is the attractive force between protons and neutrons,

namely the strong nuclear force responsible for binding the particles together. The study of the GDR provide information on the nuclear symmetry energy, on the symmetry potential, or the velocity dependence of the effective interaction. Two models of the GDR are illustrated in Fig.3.1.

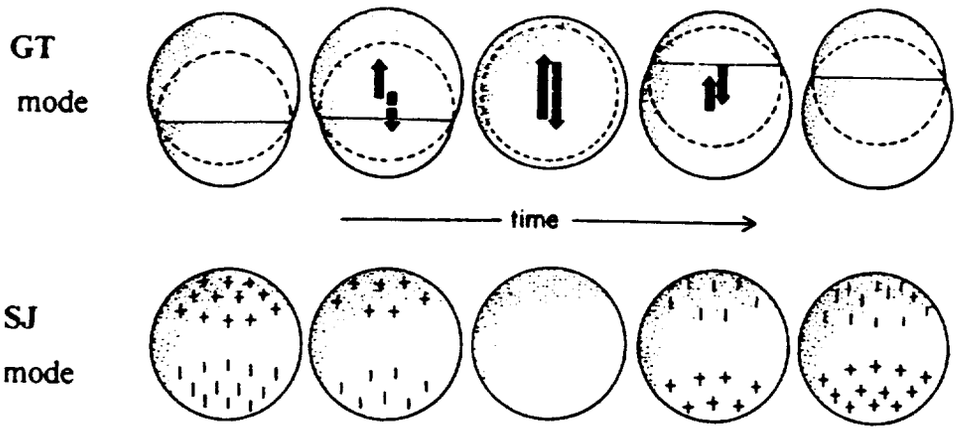

Fig.3.1. The two models of the GDR.

On the basis of few early experiments Goldhaber and Teller discussed three possible macroscopic explanations for the A dependence of the resonance energy. The first postulated an elastic binding of the neutrons to the protons that would result in a resonance energy independent of A. The second proposal, later elaborated by Steinwedel and Jensen (The SJ mode), was that the resonance might consist of density vibrations of the neutron and proton fluids against each other with the surface fixed. This kind of motion, would result in a resonance energy proportional to $A^{-1/3}$. Their third suggestion, one that they chose to discuss in some detail (the GT mode), was that the neutrons and protons might behave like two separate rigid but interpenetrating density distributions. The resulting resonance, consisting of the harmonic displacement of these distributions with respect to each other, would be expected to have an energy dependence proportional to $A^{-1/6}$. The schematic drawings shown in Fig.3.1 serve to illustrate the general features of the GT and SJ modes. For each case, one-half cycle of the vibration is shown as a function of the time. In the GT mode a uniform proton distribution (the smaller sphere whose motion is indicated by the solid arrow) vibrates against the neutron distribution. in the SJ mode the neutrons tend to pile up first on one side of the nucleus and then to the other (density excess is indicated by plus signs and

density reduction by minus signs). The protons (not shown) move in the opposite direction so the total density remains uniform [My77].

The next vibration to be reported in the early 1970's was the Giant Quadrupole Resonance (GQR). It was observed in experiments with inelastically scattered electrons, protons, ^{3}He and alpha particles. The quadrupole, unlike the dipole, is a shape vibration, in which the shape of the nucleus as well as the distribution of the nucleons changes. A nucleus vibrating in the quadrupole mode is distorted from a spherical shape to an ellipsoidal shape and moves back through a spherical shape to an ellipsoidal shape of another orientation. Here protons and neutrons are vibrating in phase and the corresponding resonance is denoted as an isoscalar one ($\Delta T=0$). There are several advantages to choosing nuclear projectiles to excite isoscalar giant modes. The principal interaction in such events is mediated by strong nuclear force, which is charge symmetric, that is the same for protons and neutrons. The charge symmetry makes it easier to excite vibrations such as the quadrupole in which the protons and neutrons move together. Vibrations in which protons move opposite to neutrons, such as the dipole, are not excited at all by charge-symmetric forces. From the study of the giant quadrupole resonance we learn about the effective masse of a nucleon in nuclear matter.

The third nuclear vibrational mode to be observed, the giant monopole vibration (GMR) is excited and detected in much the same way as the giant quadrupole. The monopole vibration is a «breathing» mode: the nucleons move inward and outward from the center of the nucleus in phase with one another ($\Delta T=0$), so that the nucleus expands and contracts. The frequency of this mode is directly related to the compressibility of the nucleus, and determination of the energy of the GMR permits the determination of the nuclear compressibility.

It is usual to classify the giant multipole resonances according to the basic oscillations of the nucleus. The electric modes are characterized by oscillations without any differentiation of spin ($\Delta S=0$). Such an example of classification is shown in Fig.3.2 for the electric ($\Delta S=0$) monopole and quadrupole resonance. The isoscalar ($\Delta T=0$) modes are characterized by oscillations of the nucleus as a whole in which protons and neutrons move in phase. The isovector ($\Delta T=1$) modes are characterized by oscillations in which protons and neutrons move out of phase without spin differentiation. The magnetic modes are characterized by oscillations that differentiate spin or angular momentum ($\Delta S=1$) rather than charge. In the magnetic isoscalar vibrations protons and

neutrons with spin up oscillate against protons and neutrons with spin down, while in the magnetic isovector modes, protons with spin up and neutrons with spin down oscillate against neutrons with spin up and protons with spin down.

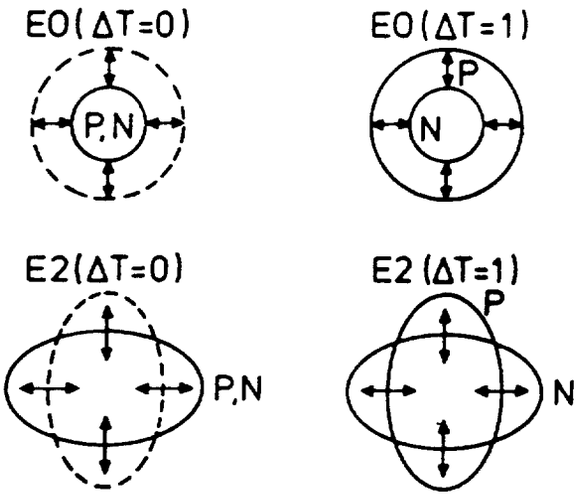

Fig.3.2. The quadrupole (E2) and monopole (E0) modes are shown. If the protons and neutrons are vibrating in phase, the corresponding resonance is denoted as the isoscalar one (ΔT=0). If the proton neutron oscillations are opposite to each other, like in the electric dipole case, the mode is called isovector (ΔT=1).

Until now we have presented a macroscopic picture of the giant resonances. It is well known however that giant resonances can also be described microscopically on the basis of the shell model. Fig.3.3 shows that the basic transitions take place between oscillator shells and can be classified according to the number of oscillator quanta involved in the transitions that describe the collective excitation. For example, the electric quadrupole excitation can involve transitions of both the $\Delta N=0$ and the $\Delta N=2$ type. In fact microscopically, giant resonances are described as a coherent superposition of 1 particle 1 hole (1p-1h) excitations. In a schematic model, the residual particle hole interaction gives rise to the formation of one strongly collective state which is a superposition of all possible 1p-1h transitions. Since the residual interaction is attractive for isoscalar and repulsive for isovector states, the corresponding collective states will be shifted up and down with respect to their unperturbed energy which is a multiple of the energy difference between two major shell, $\hbar\omega = 41A^{-1/3}$ MeV ([Ri80], page 40). For instance the energy of the giant quadrupole resonance is of $65A^{-1/3}$ for the isoscalar component and of $130A^{-1/3}$ for the isovector component.

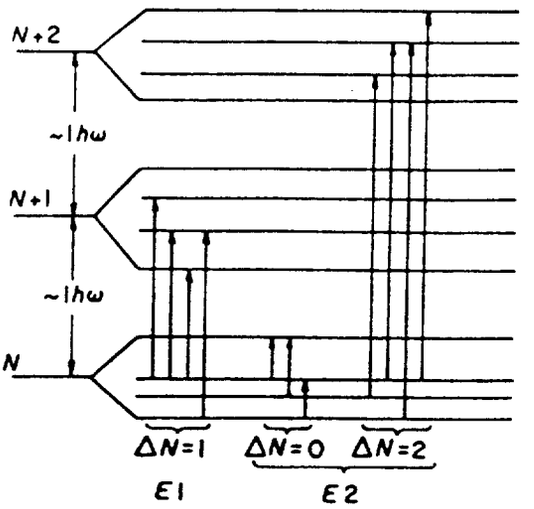

Fig.3.3. Schematic representation of E1 and E2 single particle transitions between shell model states.

With the availability of high energy proton beams, giant resonances involving spin-isospin degrees of freedom have become accessible. In 1980 Goodman et al. found that the Gamow-Teller (GTR) resonance is the dominant part of the forward angle (p,n) charge-exchange cross section [Go80]. In the meantime the spin-dipole resonance (GSDR) which involves an angular momentum transfer ΔL and a spin transfer ΔS of one unit have also been identified in (p,n) and (^{3}He,t) reactions at slightly larger scattering angles. All these collective spin-isospin modes are strongly excited in neutron rich nuclei and allow selective probing of the spin-isospin restoring forces in nuclei. A very complete discussion on this subject is given in the review articles of J. Rapaport and E. Sugarbaker [Ra94] and T.D. Taddeucci et al. [Ta87].

In 1955 Brink proposed that giant resonances can be built on all nuclear states and that their properties should not depend strongly on the details of the considered nuclear state. These giant resonances will have the same characteristics as the giant resonances built on the ground state but their energy will be shifted according to the energy of the state on which they are built. This statement in known as the Brink-Axel hypothesis [Br55].

The first observation of a giant resonance built on excited states is reported in the proton capture (p,γ) experiment on ^{11}B performed in 1964 where the GDR built on the first 2^+ state was observed.

Since this pioneering work, many experiments have shown that the GDR persists as a collective motion under extreme conditions of excitation energy and angular momentum. In our days the experimental effort in the study of giant resonances built on excited states is pursued actively towards two directions: i) study of the properties of giant resonances built on the excited states of a hot nucleus produced in heavy ion reactions, [Sn86],[Al91],[Ga92]. ii) study of the properties of giant resonances built on top of a giant mode, [Ch95].

3-2. THE GIANT DIPOLE RESONANCE

The giant dipole resonance is certainly the best studied giant mode. It has been observed in nuclei as light as ^{3}He and as heavy as ^{232}Th.

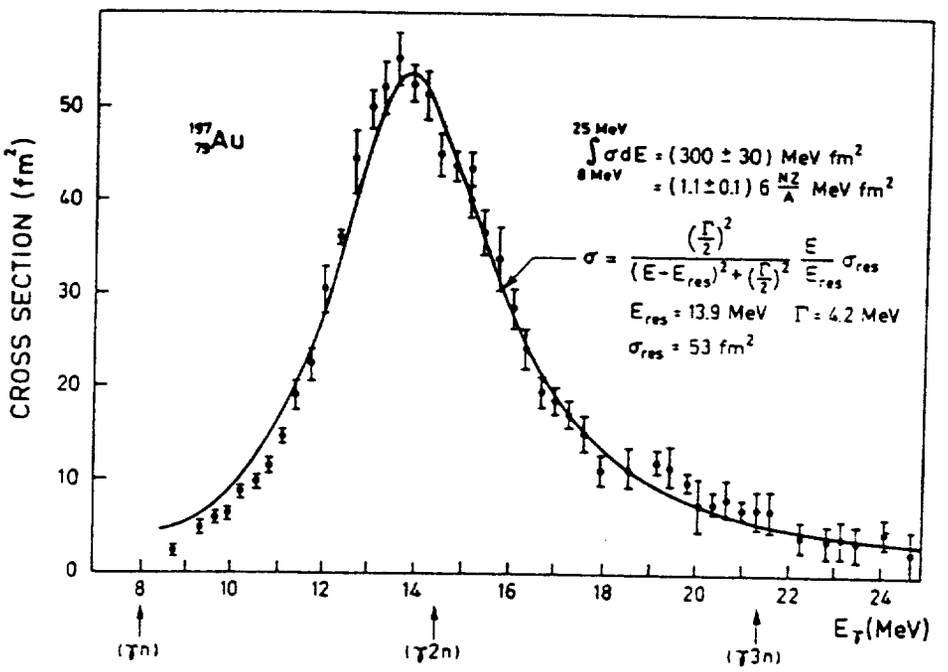

Fig.3.4. Total photoabsorption cross section for ^{197}Au. The solid curve is of Lorenz shape with the indicated parameters. (see Ref. [Bo75] page 475).

Fig.3.4 presents the photoabsorption cross section for ^{197}Au. The main decay mode of the photoexcited nucleus is by neutron emission, since the coulomb barrier inhibits emission of charged particles; thus, the absorption cross section can be deduced

from the measurement of the neutron yield. Above about 15 MeV, the (γ,2n) process contributes significantly; the magnitude of the cross section has been determined by measuring the yield of two neutrons in coincidence. For spherical nuclei the energy variation of the absorption cross section can be rather well described by a Lorentzian distribution [Bo75].

$$\sigma_{abs}(E_\gamma) = \frac{\sigma_R E_\gamma{}^2 \Gamma_{GDR}^2}{(E_\gamma^2 - E_{GDR}^2)^2 + E_\gamma^2 \Gamma_{GDR}^2} \tag{3.1}$$

where σ_R, E_γ, Γ_{GDR} are respectively the peak cross section, the resonance energy, and the full width at half maximum. For most of the studied nuclei the giant dipole resonance exhausts an important fraction of the Thomas-Reiche-Kuhn sum rule (TRK).

$$TRK = \int \sigma(E) dE = \frac{2\pi^2 e^2 \hbar}{mc} \frac{NZ}{A} \approx 60 \frac{NZ}{A} (MeVmb) \tag{3.2}$$

In fact sum rules play a very important role in giant resonance studies, since the number of participating nucleons in a transition can be measured by the fraction of the EWSR which is exhausted. The Thomas-Reiche-Kuhn sum rule is related to the classical sum rule S(E1) by the relation:

$$\text{TRK} = \frac{16\pi^3}{9\hbar c} S(E1) \tag{3.3}$$

where for a single resonance :

$$S(E1) \equiv \sum_a (E_a - E_o) B(E1; 0 \rightarrow a) \qquad \text{([Bo75] page 478)} \tag{3.4}$$

The classical sum rule is related to the more commonly used energy weighted sum rule by the relation:

$$\sum_{L=1}^{T=1} = \frac{4}{e^2} S(E1) = \frac{9\hbar^2}{2\pi m} \frac{NZ}{A} \qquad \text{([Sa83] page 601)} \tag{3.5}$$

where the super script indicates the nature of the transition T=1 or T=0, whereas the lower script is related to the multipolarity of the transition.

In nuclei with a large static deformation the GDR splits into two components corresponding to oscillations along and perpendicular to the symmetry axis. In that case, the GDR cross section is well reproduced by the sum of two Lorentzian components, see Fig.3.5.

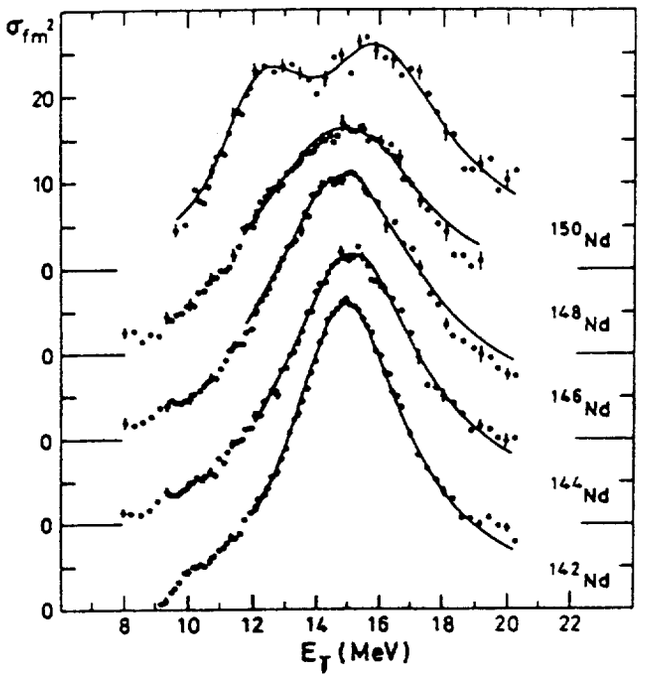

Fig.3.5. a) The photoabsorption cross section for even isotopes of Nd. (see Ref. [Bo75] page 491).

The energies of the two components are related to the deformation parameter of a prolate spheroidal nucleus by the equation:

$$\beta = \left(\frac{4\pi}{5}\right)^{1/2}\left(\frac{E_2}{E_1} - 1\right) / \left(\frac{E_2}{2E_1} + 0.8665\right)$$

For oblate nuclei the role of E_1 and E_2 is reversed [Ch87]. Both for spherical and deformed nuclei, the Lorentzian parametrisation provides a good description of the shape of the GDR in medium and heavy nuclei by treating the resonance energy, width and strength as energy independent, empirically adjustable parameters.

Using this method, it has been shown that the A dependence of the excitation energy of the dipole is intermediate between $A^{-1/3}$ and $A^{-1/6}$ and can be reproduced by a two parameter expression: $E_{GDR} = 31.2A^{-1/3} + 20.6A^{-1/6}$ MeV. However, as far as

medium and heavy nuclei are concerned, the energy of the GDR can be fairly reproduced by a simple law, $E_{GDR} = 79A^{-1/3}$ MeV [Al91]. These properties of the GDR were used to study the evolution of nuclear shapes as a function of angular momentum and temperature of a hot nucleus. It is predicted [Al86], that a rise in nuclear temperature and rotational angular momentum, by increasingly breaking down particle correlations, will drive a prolate nucleus to a triaxial and eventually to an oblate shape. Experimentally, the nuclear deformation at high spin and temperature may be obtained from splitting of the giant dipole resonance built on excited states. Measurements, performed the last decade, reported large deformation in highly excited nuclei for different mass regions. For instance D. R. Chakrabarty et al. [Ch87] have observed that highly excited Pb isotopes are deformed with $\beta \sim 0.31$. Since the Pb isotopes are nearly spherical in their ground state ($\beta \sim 0.05$) this indicated the first observation in the heavy mass region of a shape change from spherical to deformed at high excitation energies and angular momenta. The properties of the GDR built on the ground state and on excited states are shown in Fig.3.6.

Later on, the excitation of GR was studied by using strong interacting projectiles such as p, α, or more recently heavy ions. The principal interaction of those particles is mediated by the strong nuclear force, which is charge symmetric, that is the same for protons and neutrons. The charge symmetry makes it easier to excite vibrations such as the quadrupole or monopole excitation in which the protons and neutrons move together. A special case among these probes is heavy ions which interact both with the nuclear and electric field and can give rise to both isoscalar and isovector excitations. A typical example of heavy ion inelastic scattering, ^{17}O on a ^{208}Pb target, is presented in Fig.3.7. The 84 MeV/nucleon ^{17}O beam was provided by the GANIL accelerator. The scattered ^{17}O ions were detected and identified in the energy-loss magnetic spectrometer SPEG. The overall energy resolution was 800 KeV. The angular acceptance of the spectrometer covered simultaneously $1.5° \leq \theta_{CM} \leq 5.0°$. The angular accuracy is 0.05°. The absolute normalization was obtained from the target thickness and the integrated beam current measured in a Faraday cup. The error on the normalization is 10%, [Ba88]. In these analysis the GDR was parametrized by a Lorentzian with parameters obtained by photoabsorption data (E_{GDR}=13.5 MeV and Γ_{GDR}=4.0 MeV). Special attention is required in specifying the shape of the IVGDR. It is known that above 9 MeV the GDR in ^{208}Pb can be well parametrized by a Lorentz

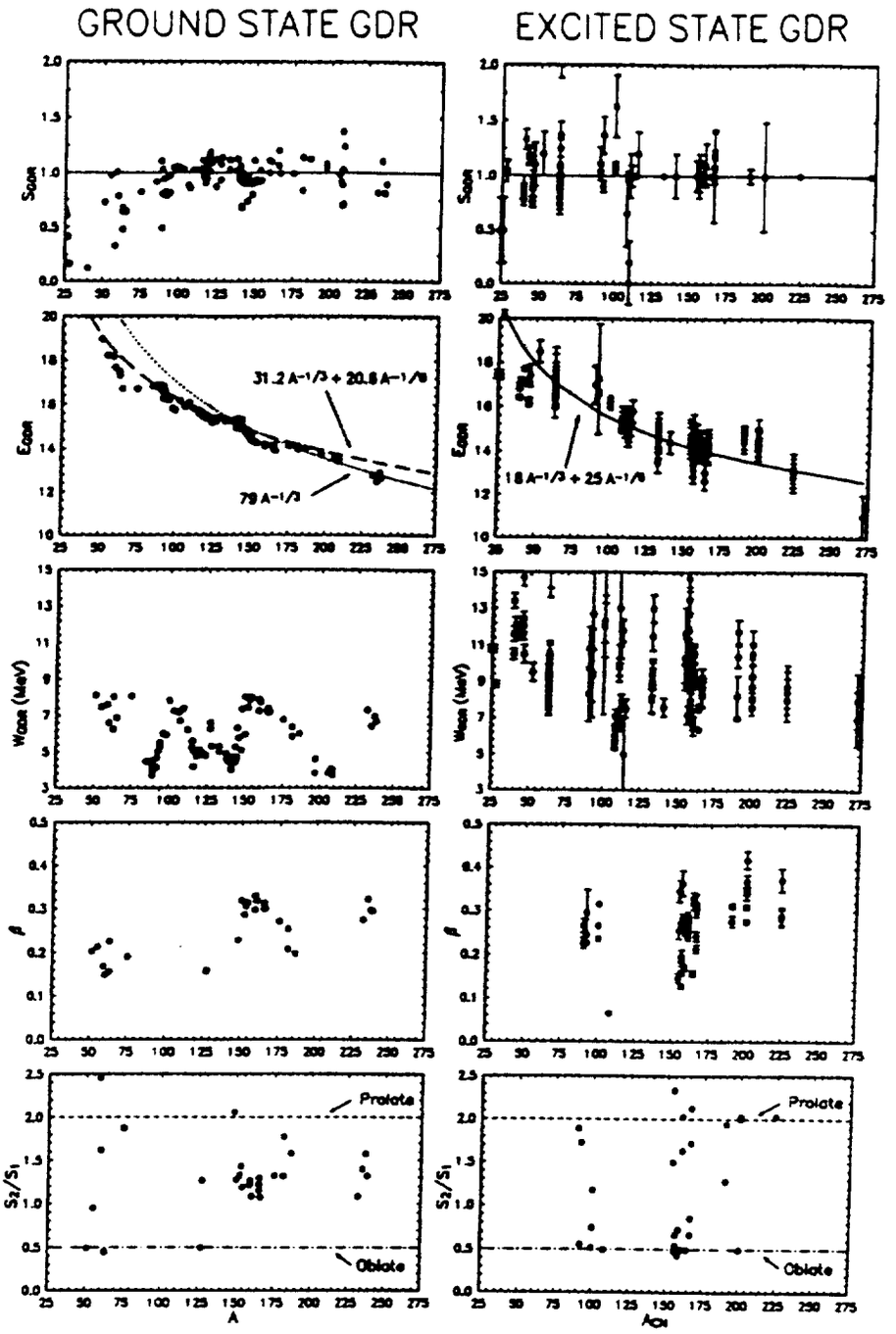

Fig.3.6. Systematic comparison of available data on giant dipole resonances in cold (left) and excited (right) nuclei as a function of mass number. From top to bottom: Strength in units of classical sum rule, centroid energy (shown are usual parametrizations of the ground state systematics and a proposed parametrisation for finite-temperature GDRs,) total width, quadrupole deformation parameter β, and strength ratio of the upper to lower components. From [Ga92]

curve centered at 13.5 MeV with a width of 4.0 MeV. However, the cross section for Coulomb Excitation of a dipole state decreases exponentially as a function of the excitation energy of that state. Thus, to properly generate the shape of the GDR peak in the inelastic spectra the strength function must be folded with this exponential probability.

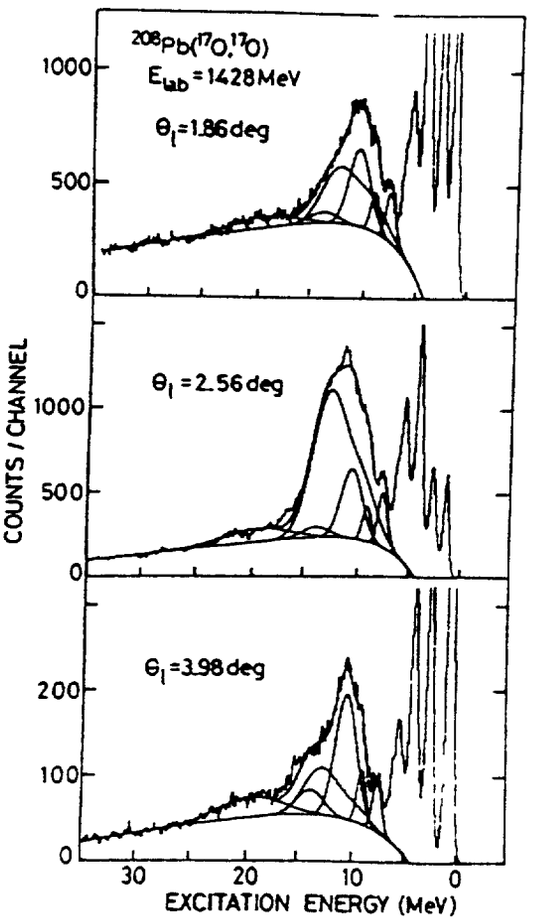

Fig.3.7. Inelastic scattering spectra at θ_{lab} = 1.86°, 2.56°, and 3.98° from the $^{208}Pb(^{17}O,^{17}O)$ inelastic scattering at 1428 MeV. The solid curves show a decomposition of the spectra into resonance peaks including the GQR and the GDR centered at 10.6 and 12.7 MeV respectively. Details on the decomposition are given in [Ba88].

The exponential dependence results in an enhancement of the low-energy portion of the GDR and shifts the position of its maximum from 13.5 MeV to 12.7 MeV. To better describe the photonuclear data at low energy, a smooth cut-off centered at E=8.3 MeV (with an width of 0.8 MeV) was applied to the assumed Lorentz strength function. The measured angular distributions for the GDR and the GQR are presented in Fig.3.8.

Special note should be made of the dramatically large values of the differential cross sections; of the order of few b/sr.

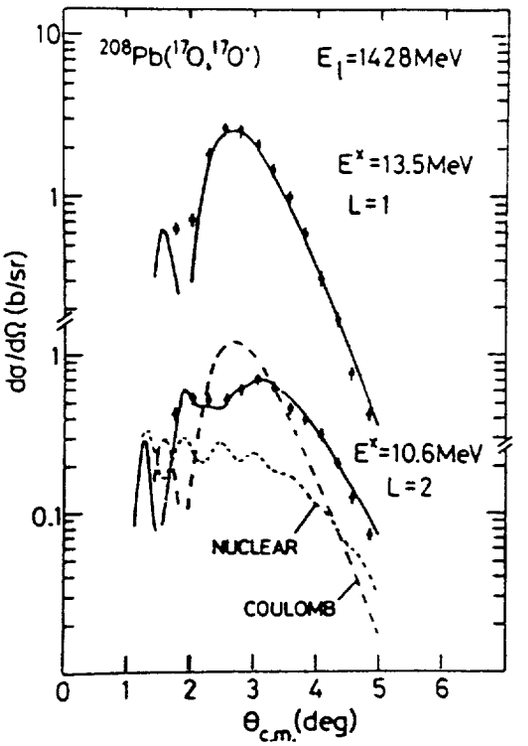

Fig.3.8. Experimental and calculated angular distributions for the isovector giant resonance (upper part) and the isoscalar giant quadrupole resonance (lower part) in ^{208}Pb. For the GQR, the calculated Coulomb and nuclear contributions to the cross section are also shown. The error bars reflect the estimated uncertainty in the fitting process and does not include the error on the absolute normalization.

The angular distributions also have distinctly different shapes; that for the GQR being broader and flatter. The inelastic angular distributions were calculated in the coupled channel formalism using standard collective form factors. The output of these calculations is the value of the deformation length $\delta=(\beta R)$ which provides the best fit of the data. The deformation length can also be related to the sum rules. The ratio $\left(\frac{(\beta R)_{exp}}{(\beta R)_{theor}}\right)^2$ of the deformation length obtained experimentally versus the deformation length obtained theoretically provides the percentage of the EWSR which is exhausted by a transition. In the case of the GDR the EWSR is,

$$\sum_{1}^{\uparrow} = \frac{4}{e^2} E_{GDR} B(E1)\uparrow = (3NZ\beta_1 R / \pi A)^2 E_{GDR} \tag{3.6}$$

From equation (3.5) and (3.6) we obtain the deformation length for the excitation of a state at excitation energy E and exhausting 100% of the EWSR.

$$(\beta_1 R)^2_{\%} = \frac{\pi A \hbar^2}{2mNZE} \tag{3.7}$$

In the calculation of the cross section for the excitation of the GDR only coulomb interaction was assumed, since the nuclear interaction is negligible. The best fit of the angular distribution corresponds to a $B(E1)\uparrow$ value which is equivalent to $110 \pm 22\%$ of the energy weighted sum rule in the energy interval 7-18.9 MeV. This agrees well with the value of 103%EWSR obtained from photonuclear studies.

In a more refined analysis the calculation of the GDR was carried out as a function of the excitation energy using a E1 strength distribution taken from photonuclear data [Be90]. Following equations (3.3) ,(3.4) and (3.6) we obtain:

$$\beta_{E1}(E) = \frac{dB(E1)\uparrow}{dE} = \frac{9\hbar c}{16\pi^3} \frac{\sigma(E)}{E} \frac{e^2 fm^2}{MeV} \tag{3. 8}$$

where $\beta_{E1}(E)$ is the distribution of E1 reduced matrix elements fixed by the photonuclear cross section $\sigma(E)$.

Special care has to be taken when calculating E1 transitions with the standard options, vibrational or rotational model, of inelastic scattering codes like ECIS [Ra81]. For these collective excitations the transition potential is given by (2.12). For the Coulomb excitation of the isovector dipole resonance the form factor is [Li93],[Sa87],

$$F_{lC}(r) = \delta_{lc} \frac{2N}{A} \frac{Z_p Z_T e^2}{r^2} \tag{3.9}$$

To obtain in these calculations the correct transition potential we should multiply the deformation parameter β obtained from (3.6 or 3.7) by a factor $\frac{2N}{A}$. Therefore:

$$\beta^{ECIS} = \frac{2.V}{A}\beta \qquad (3.10)$$

The giant resonance region in the inelastic spectra from the reaction $^{20}Ne+^{90}Zr$ and $^{20}Ne+^{208}Pb$ was also studied in a more model independent way by T. Suomijärvi et al. [Su89]. The results of this analysis are in agreement with the results of previous giant resonance decompositions.

Multiphonon states: One of the new and spectacular results in this field is the experimental discovery of multiphonon excitations, i.e. a giant mode built on the top of other giant states.

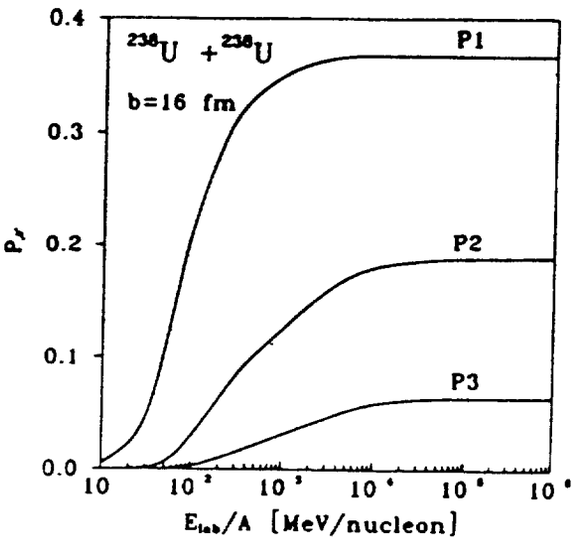

Fig.3.9. Probability to excite N phonon states in ^{238}U for the reaction $^{238}U+^{238}U$ at an impact parameter of 16 fm as a function of the laboratory energy per nucleon.

In the previous section we have shown that in heavy ion inelastic scattering at incident energies around 100 MeV/nucleon the Coulomb interaction plays a major role and that the inelastic spectrum is dominated by the dipole transition. Coulomb excitation will be even more enhanced by using heaviest beams at higher incident energies. In fact, very large probabilities are expected for the Coulomb excitation of giant resonances at relativistic energies. Under such conditions, the experimental study of the excitation of multiple phonon states built on top of the GDR becomes possible.

This is illustrated in Fig.3.9 where the excitation probabilities of a multiphonon state in ^{238}U projectile incident on a ^{238}U target at an impact parameter of 16 fm and as a function of the laboratory energy per nucleon is plotted. One observes that, at energies above a few GeV per nucleon, the excitation probabilities become constant and that the probability to excite a two phonon state in a grazing collision is only a factor 2-3 smaller than the probability to excite a one-phonon state. For larger impact parameters this factor increases considerably [Va90]. For the observation of these states two different methods have been proposed so far. The first is to study the photon decay of these states while the second is the exclusive measurement of the electromagnetic dissociation of a projectile or target nucleus in peripheral heavy ion collisions.

Photon decay measurements: The $^{209}Bi+^{208}Pb$ reaction has been studied at SIS at 1 GeV/nucleon. The photons from the decay of the GDR and the double GDR ($GDR \otimes GDR$) were detected by TAPS. TAPS consists of two towers of 128 BaF_2 detectors. Each detector is equipped with an individual charged particle veto detector. A forward wall which is a large area plastic detector records charged particles emitted in a cone between 1° and 30° in the forward direction. Peripheral events can be selected by requiring that the forward wall detects no charged particles. Since both the projectile and the target can be excited by the Coulomb field, it is crucial to be able to separate the GDR photons from both partners. For that, photons were detected at backward angles where photons from projectile decay are Doppler shifted to much lower energies than those emitted by the GDR excited by the target, which are not shifted. Therefore, projectile γ rays do not contribute significantly to the energy range of the target decay [Ri93], [Ch95]. In Fig.3.10, the γ energy spectrum from ^{208}Pb for peripheral events as defined previously, is displayed. In this spectrum, a structure at about 13 MeV, which is independent of the observation angle, clearly shows up and can be assigned to the γ decay of the GDR in ^{208}Pb. The giant resonance peak is extracted by subtracting a background parametrized as the sum of two exponentials, on each side of the observed peak, with slopes fixed by the data. The position and the width of the GDR excited in ^{208}Pb are, respectively, about 13 MeV and 4 MeV in agreement with the results of photoabsorption measurements.

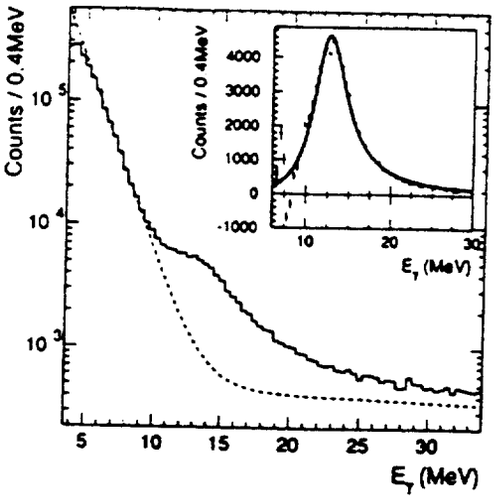

Fig.3.10. Photon energy spectrum measured for peripheral events from the $^{209}Bi+^{208}Pb$ reaction. The structure around 13 MeV corresponds to the γ decay of the Coulomb excited GDR in the ^{208}Pb target. The insert shows a Lorentz fit to the difference between the data and the background (see Ref. [Ri93]).

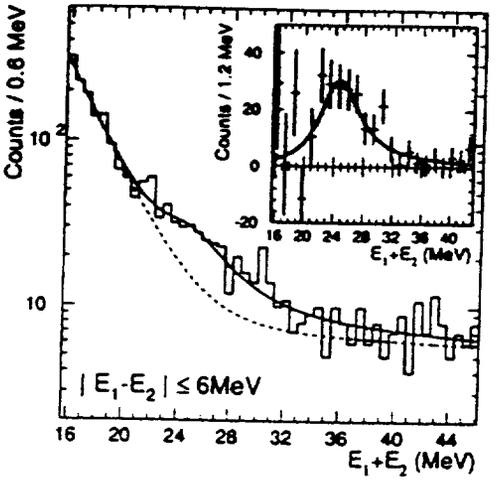

Fig.3.11. Measured double photon spectra. Sum energy of coincident photon pairs with an energy difference less than 6 MeV for peripheral events. The structure around 26 MeV is assigned to the double γ decay of the GDR⊗GDR (see Ref. [Ri93]).

A spectrum obtained by requiring coincidences of two-γ rays with an energy difference of less than 6 MeV is displayed in Fig.3.11. A broad structure at a mean energy of about 26 MeV is observed and can be attributed to the double γ decay of the *GDR⊗GDR* state. The position and the width of this structure fitted by a Lorentzian shape are found to be respectively 25.6 MeV and 5.8 MeV. These values are in

agreement with what is expected for a two phonon state. Under the assumption that the γ ray branching ratio for each phonon is independent of the number of phonons, the cross section is twice as large as the theoretical predictions.

Coulomb dissociation measurements: Experimental investigations of the fragmentation of relativistic nuclei following electromagnetic excitation have been carried out recently in order to study multiple electromagnetic excitations. As mentioned before, the aim of these experiments is to excite with a large probability high lying collective modes in the projectile using peripheral heavy ion collisions, to measure in coincidence the subsequent neutron and γ decay of these states and to construct the excitation energy of the projectile [Sc93].

The experiment was performed at the SIS facility using a ^{136}Xe beam at 0.7 GeV/nucleon on a ^{208}Pb target. The resulting excitation spectrum from ^{136}Xe obtained with ^{208}Pb and ^{12}C targets is displayed in Fig.3.12. The experimental results are compared to theoretical calculations. In these calculations, the contribution of the dipole and of both the isoscalar and isovector quadrupole resonances is taken into account. The results obtained using a C target are used to estimate the nuclear cross section. A very small contribution of such excitation for the ^{208}Pb target has been deduced showing that the measured cross section is mainly due to electromagnetic excitation. In the experimental spectrum, a structure which is assigned to the double-GDR, is clearly observed at 28 ± 1 MeV with a width of about 6 ± 2 MeV, in agreement with what is expected for a two phonon state. Its cross section however, is approximately twice the value predicted by the theoretical calculations. In a new experiment the double phonon excitation was studied for the ^{208}Pb+^{208}Pb reaction at 650 MeV/nucleon (lower right part of Fig.3.12). The cross section of excitation of the double-GDR is in agreement with the value measured with the detector TAPS, and twice the theoretical predictions. In fact the theoretical understanding of the cross section of double giant dipole resonance excitations in heavy ion reactions, remains at present a puzzle. One of the fundamental questions related to multi-phonon excitations is that of the nuclear response to an induced collective motion of increasing amplitude. One of the motivations is to explore to which extent standard theoretical methods, developed for small amplitude motions are still appropriate in the case of multiphonon excitations.

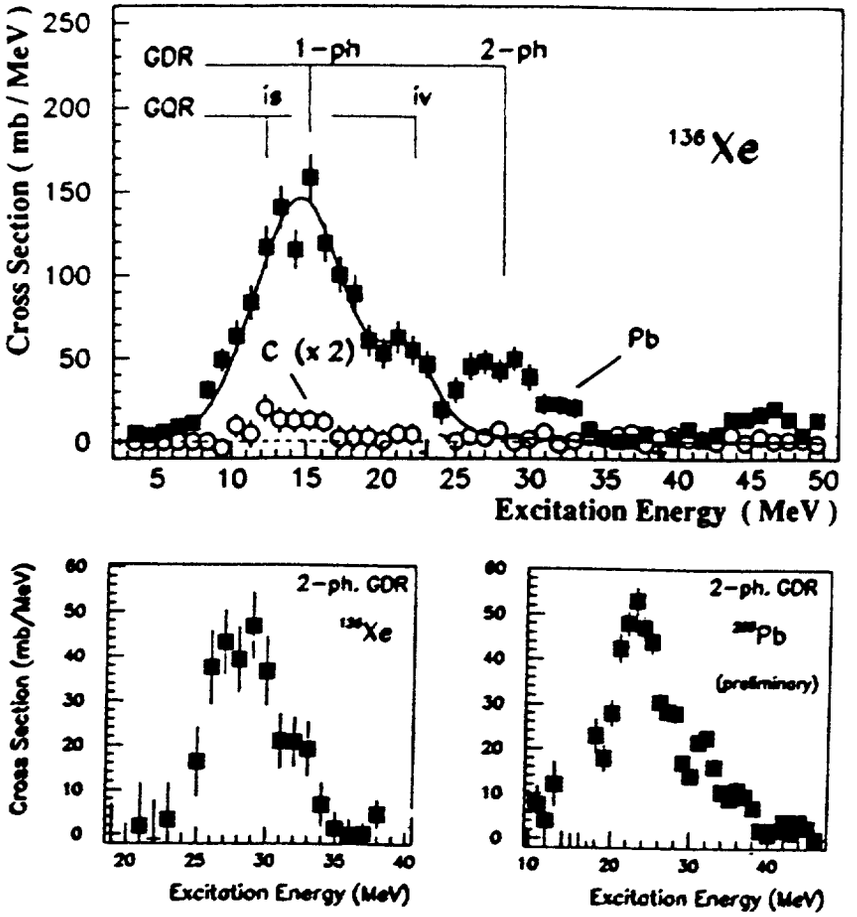

Fig.3.12. (upper part) Spectrum of ^{136}Xe (projectile) excitation on a ^{208}Pb target and on a C target; the later one is scaled by a factor two. The resonance energies for the one and two phonon GDR and for the isoscalar and the isovector GQR are indicated. The solid curve reflects the results of theoretical calculations for one phonon excitations in the Pb target.

(lower left part) Same as upper part, after subtracting the theoretical calculation for one phonon excitations.

(lower right part) same as left part, for the excitation of ^{208}Pb (650 MeV/nucleon) on a Pb target [Em94].

Concomitantly, multipohonon excitations can be used to produce exotic states of nuclear matter. Fig.3.13 displays calculated proton and neutron densities for n=4 phonon state in ^{238}U and for an n=6 phonon state in ^{40}Ca at the turning point of the dipole vibration [Em94]. Because of the large instantaneous neutron excess, it was speculated that exotic decays may occur, i.e. neutron cluster emission or two clusters of proton and neutron matter.

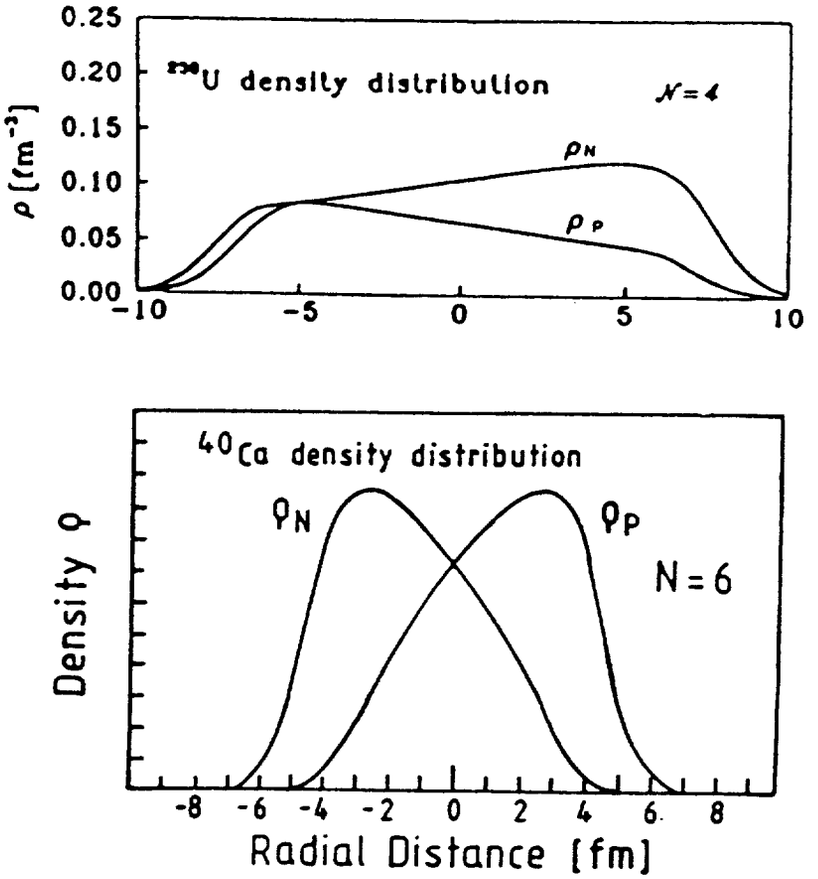

Fig.3.13. Proton and neutron densities at their distance of their largest separation calculated in the nuclear droplet model. Upper panel is for a N=4 phonon GDR state in ^{238}U, lower panel for N=6 phonon GDR state in ^{40}Ca [Em94].

3-3. THE GIANT QUADRUPOLE RESONANCE

It was as late as 1972 that the giant quadrupole resonance (GQR) was observed for the first time. Today, the properties of the isoscalar GQR are well understood from a large number of different experiments using hadron and electron beams (see for example [Be76,Wo91]). The various data reported in Fig.3.14 coming from proton, α or electron scattering experiments show that the results obtained using different probes are in good agreement.

The energy weighted sum rule for the excitation of a giant mode with multipolarity $l \geq 2$ is:

$$\sum_{l}^{0} = \sum_{l}^{1} = \left(\frac{\hbar^2}{8\pi m}\right) A l(2l+1)^2 \left\langle r^{2l-2} \right\rangle_{\rho} = \sum_{a} \frac{1}{e^2} (E_a - E_0) B_a(El)\uparrow \qquad (3.12)$$

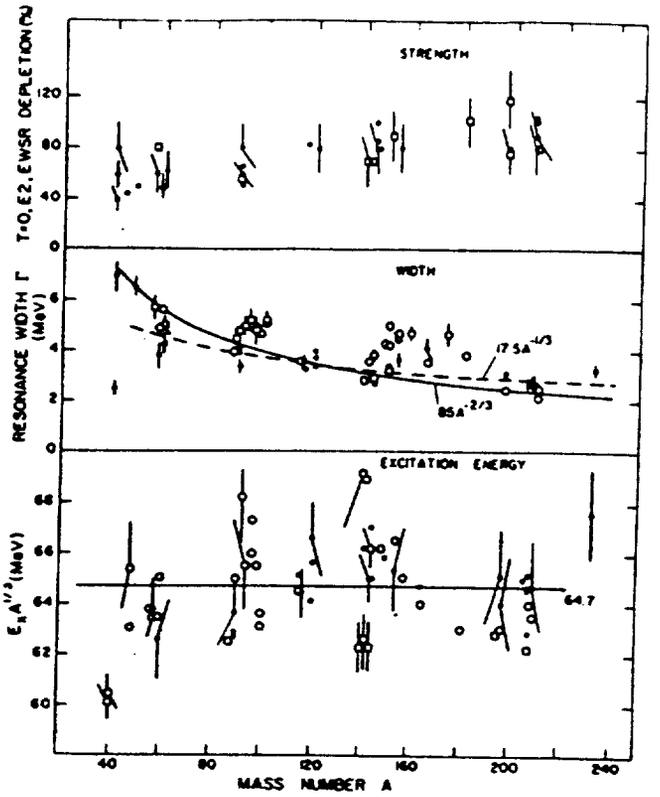

Fig.3.14. Properties of the GQR Systematics for the excitation energy, width Γ and fraction of the energy weighted sum rule strength of the isoscalar giant quadrupole resonance presented as a function of the nucleus mass [Wo91].

where the average is taken over the ground state mass distribution ρ(r). For an uniform distribution of radius R_0: $\left\langle r^{2l-2} \right\rangle = 3R_0^{2l-2}/(2l+1)$ and $B_a(El)\uparrow$ is the usual El reduced transition probability ([Sa83],(14.70b)).

$$B_a(El)\uparrow = \left[\frac{3AR_0^l\beta}{4\pi}\right]^2 \qquad (3.13)$$

From equations (3.12) and (3.13) we obtain the deformation length for a state of an excitation energy E exhausting 100% of the El EWSR.

$$(\beta_l R)^2_{100\%} = \frac{2\pi\hbar^2}{3AmE} l(2l+1) \qquad (3.14)$$

For nuclei with A>40, 50-100% of the E2 EWSR has been localized in a peak at about $65A^{-1/3}$ MeV. Its width varies from 6 to 2.5 MeV for nuclei from Ca to Pb. For lighter nuclei, the isoscalar GQR is highly fragmented. Another important fraction of the EWSR is exhausted by the low energy 2^+ state. In fact, it has been found experimentally that the low-lying 2^+ state usually exhausts about 10-20% of the EWSR.

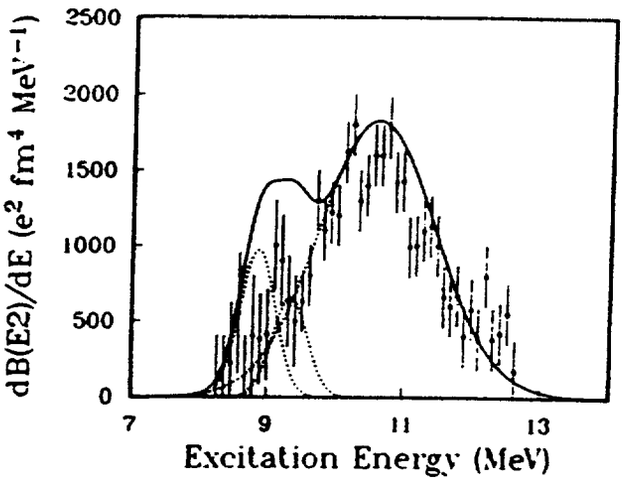

Fig.3.15. Distribution of $B(E2)\uparrow$ in the GQR region in ^{208}Pb obtained from (e,e'n) and heavy ion inelastic scattering.

The energy of the giant quadrupole resonance obtained in theoretical calculations for a value of the nucleon effective mass of m*=0.75m,

$$E_{GQR} = \sqrt{2}\hbar\omega\sqrt{\frac{m}{m^*}} = 67A^{-1/3} \text{ MeV}$$

is in good agreement with the experimental result $E_{GQR}= 65A^{-1/3}$. It should be recalled that calculations of nuclear matter which start from realistic nucleon-nucleon interactions always give effective masses, for particles near the Fermi surface, of: m*~(0.65-0.75)m [Br80].

An interesting new development is the observation that in inelastic scattering of fast heavy ions at small angles, giant resonances are excited with large cross sections

and favorable resonance to continuum ratio [Ba88]. The dominant excitation process in this case is Coulomb-excitation, which implies that, as in electron scattering, isoscalar and isovector resonances are equally well excited. This is illustrated in Fig.3.7 and Fig.3.8. The quality of the data and the fact that the GQR is electromagnetically excited, allow for a direct comparison of the distribution of B(E2)↑, as shown in Fig.3.15. The data points are from the (e,e'n) data of Ref. [Bo88] while the solid line is the $B(E2)\uparrow$ distribution obtained by Been et al. [Be90]. Are included the contribution of the 8.8 and 9.3 MeV E2 states for which the B(E2)↑ values were obtained experimentally. It is clear from Fig.3.15 that not only the integrated B(E2) strength, but also the distribution of B(E2) strength is in excellent agreement for the two data sets. These results provide the energy, width and shape of the GQR in ^{208}Pb and are certainly the best available results today concerning the GQR excitation. We would like to notice that sophisticated Hartree-Fock calculations using the Gogny D1S interaction predict the GQR in ^{208}Pb at 12 MeV [De94], instead of 10.6 MeV.

Multiphonon states: Aside from the double-GDR, evidence for two-phonon states has been reported so far only for the isoscalar quadrupole resonance. In fact the most convincing signature on the multiphonon excitation of the GQR was obtained recently at GANIL for the ^{40}Ca+^{40}Ca system at 50 MeV/nucleon [Sc93a]. Inelastically scattered Ca projectiles, analyzed with a magnetic spectrometer were detected in coincidence with protons emitted at backward angles to favor the selection of target excitations in the inelastic spectrum, since other mechanisms such as pickup, breakup, and knockout give rise to forward peacked protons. Fig.3.16 exhibits a prominent structure centered around 34 MeV excitation energy. In the inclusive spectrum not shown here, a peak at 17.5 MeV and a weaker component centered at 14. MeV are observed, both being ascribed to an excitation of the single isoscalar GQR. As appearing at about twice the GQR excitation energy, the peak at 34 MeV in the proton coincident spectrum is assigned to the two-phonon state. The assignment is supported by a detailed study of the proton decay characteristics. Like for the excitation of the double-GDR theoretical calculations underestimate the double-GQR cross section by a factor of about two. These measurements prove that heavy ion inelastic scattering in combination with coincident decay measurements is a powerful tool to investigate multiphonon states.

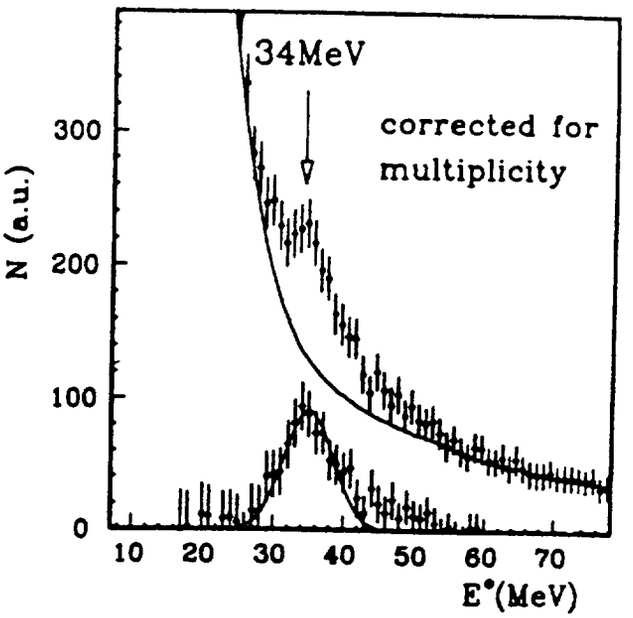

Fig.3.16. Inelastic spectrum corrected for the proton multiplicity. The solid line corresponds to a polynomial fit of the background. The result of the background subtraction is shown below, fitted by a Gaussian [Sc93a].

3-4. THE GIANT MONOPOLE RESONANCE

The existence of the electric isoscalar giant monopole resonance (GMR) in medium and heavy nuclei was first established in 1977. The giant monopole resonance GMR is the L=0 mode and is the only volume oscillation which has been isolated. The frequency of this breathing mode is directly related to the compressibility of the nucleus and the determination of its energy is the most direct way to access to the compressibility of nuclear matter. A large amount of data has been obtained from (α,α) and (^{3}He,^{3}He) inelastic scattering , which locate the GMR at nearly $80A^{-1/3}$ (see Fig. 3. 17).

The nuclear matter compressibility is defined as,

$$K_{nm} = 9\rho_0 \frac{d^2 E/A}{d\rho_0^{\,2}}$$

where ρ_0 is the saturation density.

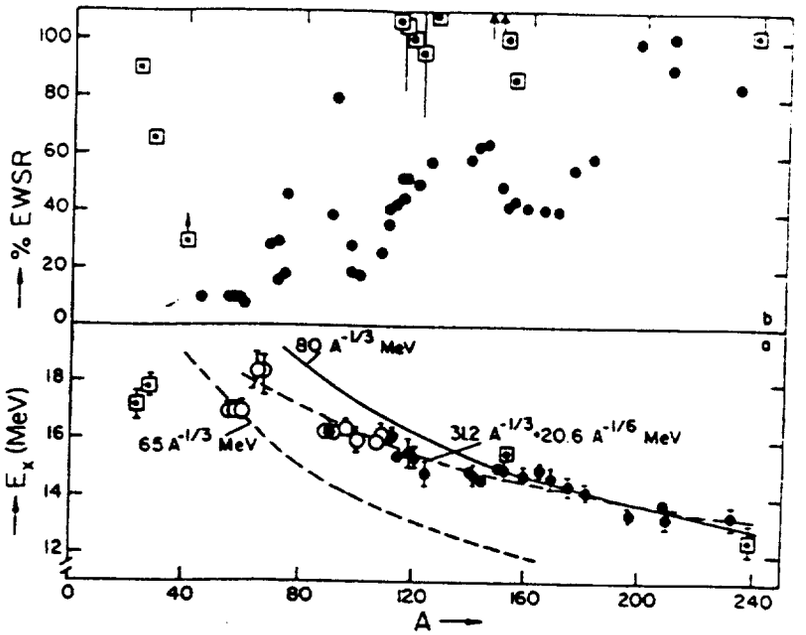

Fig.3.17. Systematics of the isoscalar GMR: a) The centroid energy as a function of the mass A and (b) the fraction of the energy weighted sum rule observed to be exhausted. The curve indicated by ($31A^{-1/3}+20.6A^{-1/6}$) MeV valid for the GDR (Fig.3.6), shows that for nearly all the nuclei the GMR and the GDR coincide in excitation energy. The curve indicated by $65A^{-1/3}$ MeV valid for the GQR indicates that for A~60 the GMR and the GQR happen to coincide (for details see Ref. [Wo91]).

The starting point for obtaining the nuclear matter compressibility is an expansion of the compression modulus of a nucleus K_A inspired from the liquid drop formula. That is, one separates volume, surface, symmetry and Coulomb contributions by writing

$$K_A = K_{vol} + K_{surf}A^{-1/3} + K_{sym}\left(\frac{N-Z}{A}\right)^2 + K_{coul}\frac{Z^2}{A^{4/3}} + \ldots\ldots \qquad (3.15)$$

where N and Z are respectively the numbers of neutrons and protons and A=N+Z. In the scaling model the nuclear matter compression modulus K_{nm} is identified with the volume term K_{vol} [Bl95]. In order to obtain from this expression K_{nm} one has to perform a least-square fit using the values of K_A derived from the excitation energy E_0 and the width Γ of the GMR and which are related by the following expression.

$$E_0^2 = \hbar(\frac{K_A}{m < r_0^2 >}) - 3(\frac{\Gamma}{2.35})^2 \qquad (3.16)$$

This expansion or more sophisticated versions of this expansion have been widely used to obtain the saturation properties of nuclear matter [Na95],[My95],[Sh93]. This procedure presents however conceptual and practical difficulties [Bl95]. Indeed the A dependance of K_A is rather weak. Besides, in the range of the relevant nuclei, those in which the breathing mode is well identified as a collective excitation, $A^{-1/3}$ varies only slightly. The difficulty of obtaining reliable values for the various parameters by a straigtforward fit of the data was illustrated by Pearson [Pe91], who showed that equally good fits can be obtained with the volume term taking arbitrary values in a wide range, $100 < K_{vol} < 400$MeV. To overcome these difficulties Blaizot et al. [Bl95] have used a microscopic approch to obtain the nuclear matter compressibility from the available experimental data for ^{208}Pb. The microscopic determination of the nuclear matter compressibility relies on the possibility of constructing sets of effective interactions which differ mostly by their predictions of K_{nm} and which otherwise provide good fits to other nuclear properties. Fig.3.18 summarize the results of these calculations. The energy of the breathing mode is presented as a function of K_{nm}. The circles indicate the values of the GMR energy obtained from a constrained Hartree-Fock calculation. The diamonds correspond to the average value of the energy of the RPA strength distribution. The dashed line is a square root fit to the Hartree -Fock values. Experimental values and their error bars are indicated by small rectangles near the vertical axis. These are, in MeV: $E_0 = 13.70 \pm 0.40$ (TAMU), [Yo81]; $E_0 = 13.90 \pm 0.30$ (Groningen), [Br87]; $E_0 = 13.20 \pm 0.30$ (Grenoble), [Bu80]. All available data point to a value of K_{nm} smaller than 240 MeV. It is important to notice that the main uncertainty of the final value of K_{nm} comes from the present uncertainties in the data. There is a systematic difference between the three sets of data reported here. Since $E_0 \sim K_{nm}$, and K_A varies linearly with K_{nm}, $\delta K_A / K_A = 2\delta E_0 / E_0 = dK_{nm} / K_{nm}$, so that an error $\delta E_0 \sim 1$ MeV traslates into an uncertainty on K_{nm} of about 25 MeV. Groningen data lead to K_{nm} ~230 MeV, and Grenoble data to K_{nm} ~205 MeV. Following these calculations the main source of uncertainty is the lack of compatible and precise data in heavy nuclei. Taking into account all the experimental results, it is clear from the previous analysis that $207 < K_{nm} < 225$ MeV.

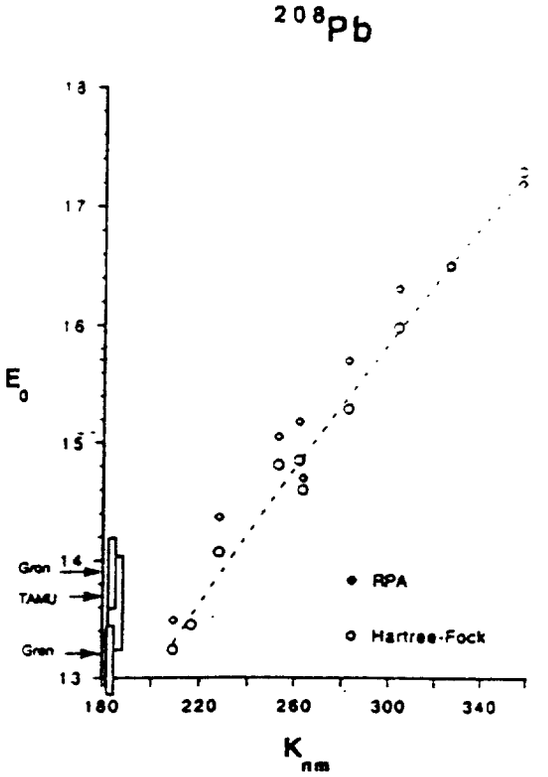

Fig.3.18. The energy of the breathing mode as a function of K_{nm}, for details see Ref. [Bl95]

The giant monopole mode was extensively studied in light-ion inelastic-scattering measurements and the observed strength seems to decrease almost linearly from about 100% of the E0 EWSR in A > 160 nuclei to about 10% in nuclei with A~60 (see Fig.3.17). However this picture seems today questionable because recent charged-particle decay studies of giant modes revealed the presence close to 100% of E0 strength in nuclei with A~24,28 [To90],[Lu86]. The heavy-ion inelastic scattering data of [Li93] sow that an important fraction of the E0 strength is also exhausted for intermediate mass nuclei. The apparent disagreement may be attributed to the difference between the reaction mechanism of the two probes. For instance heavy-ion inelastic scattering provides spectra with much larger peak-to-continuum ratios, which makes heavy ions suitable probes for these studies. Furthermore, light- and heavy probes are sensitive to different radial parts of the E0 transition potential. This situation reminds the discussion on folding transition potentials for describing inelastic scattering measurement §2-4. The same kind of comparison was made in the case of the targets ^{60}Ni, ^{90}Zr, ^{120}Sn and ^{208}Pb for the excitation of the giant quadrupole resonance and giant monopole resonance by ^{17}O ions at 84MeV/nucleon [Ho95]. The resulting estimates of the sum-rule exhaustion by the giant quadrupole resonance increase by

amounts ranging from about 20% for the lighter targets to no change for ^{208}Pb, when the folding model is used. Applying the same model to data for excitation of the giant monopole resonance, it was found [Ho95] that these transitions overexhaust the corresponding sum rule even more than was previously found within the deformed potential optical model [Li93]. This situation may be due to deficiencies in the simple Tassie model of the transition density that was used in the case of the giant resonances, although several nuclear structure calculations lend support to this form. An alternative suggestion is that the presence in the extracted cross sections of a background of excitations with other multipolarities, especially l=4, is responsible for the discrepancies. An l=4 excitation with a strength of only 10 to 15% of the hexadecapole sum rule limit has cross sections comparable to the monopole with 100% strength. This difficulty may be overcome by 0° heavy-ion inelastic scattering measurements, in which a cleaner separation of different multipolarities is expected and which could also provide a better determination of the energy of the GMR and therefore a better determination of the nuclear compressibility.

OUTLOOK

In this paper we have discussed some aspects of nuclear elastic and inelastic scattering. The paper contains a short review of the field with special emphasis on more recent results and problems concerning intermediate energy heavy ion elastic and inelastic scattering. Nowadays the experimental effort in this field is pursued actively towards the study of the properties of giant resonances built on top of a giant mode and mainly on the study of the properties of exotic nuclei. Indeed, with the recent advent of unstable nuclear beam facilities, these studies gained new interest, since it becomes now possible to study elastic and inelastic scattering for nuclei lying far from stability. The weak binding energy of these species is expected to lead to modifications of standard optical potential models which were developed for stable nuclei. Inelastic scattering experiments may allow to study in detail the halo structure of the nuclei and to obtain their ground state deformation as this was shown for a pioneer experiment in §2-3. A characteristic of some exotic nuclei is to exhibit density distributions different from stable nuclei. In particular, the differences between neutron and proton density distributions give rise in light nuclei to a neutron halo and in heavier ones to a neutron skin. Well known collective modes like the GDR are a useful tool to explore these phenomena. For instance, the cross section for GDR excitation by an isoscalar probe depends on the thickness of the neutron skin [Kr94]. This effect might be used to determine the skin thickness in exotic nuclei in inverse reaction kinematics. The study of the GMR in isobaric or isotopic chains of nuclei including unstable ones is of interest since its peak energy is directly related to the nuclear compressibility and as such is a stringent test of effective interactions used in microscopic models.

In conclusion, one can say that elastic and inelastic scattering is still a large and fascinating field where new experimental results and theoretical debates are expected in the near future.

The authors would like to thank Pr. J. Barrette for many enlightening discussions and for his careful reading of the manuscript. We would like to thank also V. Lapoux for her interest in this work and for pointing out some errors in the formulae.

References

[Al84] N. Alamanos, F. Auger, J. Barrette, B. Berthier, B. Fernandez, J. Gastebois, L. Papineau, H. Doubre and W. Mittig, Phys. Lett. **137B** (1984) 37.

[Al86] Y. Alhassid, S. Levit and J. Zingman, Phys. Rev. Lett. **57** (1986) 539.

[Al91] N. Alamanos et F. Auger, Ann. Phys. Fr. **16** (1991) 41.

[Az85] M. El-Azab Farid and G.R. Satchler, Nucl. Phys. **A441** (1985) 157; and M. El-Azab Farid and G.R. Satchler, Nucl. Phys. **A438** (1985) 525.

[Ba77] R.C. Barrett and D. Jackson, Nuclear Sizes and Structure (Clarendon press-Oxford 1977) and D. Jackson, Nuclear Reactions (Methuen and Co LTD 1970).

[Ba88] J. Barrette, N. Alamanos, F. Auger, B. Fernandez, A. Gillibert, D.J. Horen, J.R. Beene, F.E. Bertrand, R.L. Auble, B.L. Burks, J. Gomez Del Campo, M.L. Halbert, R.O. Sayer, W. Mittig, Y. Schutz, B. Haas and J.P. Vivien, Phys. Lett. **209B** (1988) 182.

[Be76] F.E. Bertrand, Ann. Rev. Nucl. Part. Sci. **26** (1976) 475.

[Be77] G. Bertsch, J. Borysowicz, H. McManus and W.G. Love, Nucl. Phys. **A284** (1977) 399.

[Be78] K. Bear and P. E. Hodgson J. Phys. G: Nucl. Phys. **Vol.4**, No12, 1978.

[Be81] F. E. Bertrand, Nucl. Phys. **A354** (1981) 129c.

[Be90] J.R.Beene, F.E. Bertrand, D.J. Horen, J.L. Lisanti, M.L. Halbert, D.C. Hensley, J. Barrette, N. Alamanos, F. Auger, B. Fernandez, A. Gillibert, W. Mittig, Y. Schutz, B. Haas, J.P. Vivien, A.M. Nathan, Phys. Rev. **C41** (1990) 920.

[Be93] J.R. Beene, D.J. Horen, and G.R. Satchler, Phys. Rev. **C48** (1993) 3128.

[Be95] J.R. Beene, D.J. Horen, and G.R. Satchler, Phys. Lett. **B344** (1995) 67.

[Be96] J.R. Beene, D.J. Horen, and G.R. Satchler, Nucl. Phys. **A596** (1996) 137.

[Bl95] J.P. Blaizot, J.F. Berger, J. Dechargé, and M. Girod, Nucl. Phys. **A591** (1995) 435.

[Bo75] A. Bohr and B. Mottelson, Nuclear structure (Benjamin, New York, 1975)

[Bo88] G.O. Bolme, L.S. Gardman, R. Doerfler, L.J. Koester, Jr., B.L. Miller, C.N. Papanicolas, H. Rothhaas, and S.E. Williamson, Phys. Rev. Lett. **61** (1988) 1081.

[Br55] D.M. Brink, PhD, Oxford University, unpublished (1955) and P. Axel, Phys. Rev. **126** (1962) 671.

[Br75] D.M. Brink and Fl. Stancu, Nucl. Phys. **A243** (1975) 175.

[Br77] D.M. Brink and N. Takigawa, Nucl. Phys. **A279** (1977) 159.

[Br78] F. A. Brieva and J. R. Rook, Nucl. Phys. **A307** (1978) 493 and references therein.

[Br80] G.E. Brown, Proceedings of the Giant Multipole Resonance Topical Conference, Oak Ridge, 1979, ed. F.E. Bertrand (Harwood Academic Publishers).

[Br82] M.E. Brandan, Phys. Rev. Lett. **49** (1982) 1132.

[Br86] M.E. Brandan, A. Menchaca-Rocha, M. Buenerd, J. Chauvin, P. de Saintignon, G. Duhamel, D. Lebrun, P. Martin, G. Perrin, and J.Y. Hostachy, Phys. Rev **C34** (1986) 1484.

[Br87] S. Brandeburg, W.T.A. Borghols, A.G. Drentje, L.P. Ekström, M.N. Harakeh, A. van der Woude, A. Hakansson, L. Nilsson, N. Olsson, and R. De Leo, Nucl. Phys. **A466** (1987) 29.

[Br88] M.E. Brandan and G.R. Satchler, Nucl. Phys. **A487** (1988) 477.

[Bu80] M. Buenerd, D. Lebrun, Ph. Martin, P. de Santignon, and C. Perrin, Phys. Rev. Lett. **45** (1980) 1667.

[Ch87] D.R. Chakrabarty, M. Thoennessen, N. Alamanos, P. Paul and S. Sen, Phys. Rev. Lett. **58** (1987) 1092.

[Ch95] Ph. Chomaz et N. Frascaria, Phys. Rep. **252** (1995) 275.

[Ch95b] J.A. Christley, C.H. Dasso, S.M. Lenzi, M.A. Nagarajan and A. Vitturi, Nucl. Phys. **A587** (1995) 390.

[De94] J. Dechargé and J.F. Berger, private communication

[Em94] H. Emling, Prog. Part. Nucl. Phys., Vol. **33** (1994) 729.

[Fa84] A. Faessler, W.H. Dickhoff, M. Trefz, and M. Rhoades-Brown, Nucl. Phys. **A428** (1984) 271c.

[Fu91] M. Fukuda, I. Ichihara, N. Inabe, T. Kubo, H. Kumagai, T. Nakagawa, Y. Yano, I. Tanihata, M. Adachi, K. Asahi, M. Kouguchi, M. Ishihara, H. Sagawa and S. Shimoura, Phys. Lett. **B268** (1991) 339; and I. Tanihata, T. Kobayashi, T. Suzuki, K. Yoshida, S. Shimoura, K. Sugimoto, K. Matsuta, T. Minamisono, W. Christie, D. Olson and H. Wieman, Phys. Lett. **B287** (1992) 307; and A. C. C. Villari, W. Mittig, E. Plagnol, Y. Schutz, M. Lewitowicz, L. Bianchi, B. Fernandez, J. Gastebois, A. Gillibert, C. Stephan, L. Tassan-Got, G. Audi, Wenlong Zhan, A. Cunsolo, A. Foti, A. Belezyorov, S. Lukyanov and Y. Penionzhkevich, Phys. Lett. **B268** (1991) 345.

[Fu92] N. Fukunishi, T. Otsuka, and T. Sebe, Phys. Lett. **B296** (1992) 279.

[Ga92] J.J. Gaardhoje, Ann. Rev. Nucl. Part. Sci. **42** (1992) 483.

[Ge89] H.V.von Geramb, Microscopic Optical Potentials, proceedings, Hamburg, 1978 Edited by H.V.von Geramb, Springer-Verlag **89**.

[Go80] C. D. Goodman, C.A. Goulding, M.B. Greenfield, J. Rapaport, D.E. Bainum, C.C. Foster, W.G. love and F. Petrovich, Phys. Lett. **44** (1980) 1755.

[He73] D.L. Hendrie, Phys. Rev. Lett. **31** (1973) 478.

[Ho90] D.J. Horen, F.E. Bertrand, J.R. Beene, G.R. Satchler, W. Mittig, A.C.C. Villari, Y. Schutz, Zhen Wenlong, E. Plagnol and A. Gillibert, Phys. Rev **C42** (1990) 2412

[Ho91] D.J. Horen, F.E. Bertrand, J.R. Beene, G.R. Satchler, W. Mittig, A.C.C. Villari, Y. Schutz, Zhen Wenlong, E. Plagnol and A. Gillibert, Phys. Rev **C44** (1991) 2385

[Ho95] D.J. Horen, J.R. Beene, and G.R. Satchler, Phys. Rev. **C52** (1995) 1554.

[Je77] J.P. Jeukenne, A. Lejeune, and C. Mahaux, Phys. Rev. **C16** (1977) 80 and references therein.

[Kh88] D.T. Khoa, Nucl. Phys. **A484** (1988) 376.

[Kh93] D.T. Khoa and W. von Oertzen Phys. Lett. **B304** (1993) 8.

[Kh94] D.T. Khoa, W. von Oertzen, and H.G. Bohlen, Phys. Rev. **C49** (1994) 1652.

[Kh95] D.T. Khoa, W. von Oertzen, H.G. Bohlen, G. Bartnitzky, H. Clement, Y. Sugiyama, B. Gebauer, A.N. Ostrowski, Th. Wilpert, M. Wilpert, and C. Langner, Phys. Rev. Lett. **74** (1995) 34.

[Kh96] J.S. Al-Khalili, M.D. Cortina-Gil, P. Roussel-Chomaz, N. Alamanos, J. Barrette, W. Mittig, F. Auger, Y. Blumenfeld, J.M. Casandjian, M. Chartier, V. Fekou-Youmbi, B. Fernandez, N. Frascaria, A. Gillibert, H. Laurent, A. Lepine-Szily, N.A. Orr, V. Pascalon, J.A. Scarpaci, J.L. Sida, and T. Suomijärvi, Phys. Lett. **B378** (1996) 45.

[Ko84] A.M. Kobos, B.A. Brown, R. Lindsay, and G.R. Satchler, Nucl. Phys. **A425** (1984) 205.

[Ko88] A.M. Kobos, M.E. Brandan, and G.R. Satchler, Nucl. Phys. **A487** (1988) 457.

[Ko93] A.A. Korsheninnikov, K. Yoshida, D.V. Aleksandrov, N. Aoi, N. Inabe, M. Fujimaki, T. Kobayashi, H. Kumagai, C.-B. Moon, E.Yu. Nikolskii, M.M. Obuti, A.A. Oglobin, O. Ozawa, S. Shimoura, T. Suzuki, I. Tanihata, Y. Watanabe and M. Yanokura, Phys. Lett. **B316** (1993) 38.

[Li93] R. Liguori Neto, P. Roussel-Chomaz, L. Rochais, N. Alamanos, F. Auger, B. Fernandez, J. Gastebois, A. Gillibert, R. Lacey, A. Miczaika, D. Pierroutsakou, J. Barrette, S.K. Mark, R. Turcotte, Y. Blumenfeld, N. Frascaria, J.P. Garron, J.C. Roynette, J.A. Scarpaci, T. Suomijäevi, A. Van der Woude and A.M. Van der Berg, Nucl. Phys. **A560** (1993) 733.

[Kr94] A. Krasznahorkay, A. Balanda, J. A. Bordewijk, S. Branderburg, M.N. Harakeh, N. Kalantar-Nayestanaki, B.M. Nyako, J. Timar and A. van der Woude, Nucl. Phys. **A567** (1994) 521.

[Lu86] H.J. Lu, S. Brandenbutg, R. De Leo, M.N. Harakeh, T.D. Poelhekken and A. van der Woude Phys. Rev. **C33** (1986) 1116.

[Me83] S. Mellena, R.W. Finlay, F.S. Dietrich, and F. Petrovich, Phys. Rev. **C28** (1983) 2267.

[Mo92] C.-B. Moon, M. Fujimaki, S. Hirenzaki, N. Inabe, K. Katori, J.C. Kim, T. Kobayashi, T. Kubo, H. Kumagai, S. Shimoura, T. Suzuki, and I. Tanihata, Phys. Lett. **B297** (1992) 39.

[Mo95] T. Motobayashi, Y. Ikeda, Y. Ando, K. Ieki, M. Inoue, N. Iwasa, T. Kikuchi, M. Kurokawa, S. Moriya, S. Ogawa, H. Murakami, S. Shimoura, Y. Yanagisawa, T. Nakamura, Y. Watanabe, M. Ishihara, T. Teranishi, H. Okuno, and R.F. Casten, Phys. Lett. **B346** (1995) 9.

[My73] W.D. Myers, Nucl. Phys. **A204** (1973) 171.

[My77] W.D. Myers, W.J. Swiatecki, T. Kodama, L.J. El-Jaik, and E.R. Hilf, Phys. Rev. **C15** (1977) 2032.

[My95] W.D. Myers and W.J. Swiatecki, Nucl. Phys. **A587** (1995) 92.

[Na95] R. Nayak, V.S. Uma Maheswari, and L. Satpathy, Phys. Rev. **C52** (1995) 711.

[Ne70] J.W. Negele, Phys. Rev. **C1** (1970) 1260.

[Pe85] J. S. Petler, M.S. Islam, R.W. Finlay, and F.S. Dietrich, Phys. Rev. **C32** (1985) 673.

[Pe91] J.M. Pearson, Phys. Lett. **B271** (1991) 12.

[Pr75] M.A. Preston and R.K. Bhaduri, Structure of the nucleus (reading, MA: Addison-Wesley 1975).

[Ra81] J. Raynal, Phys. Rev. **C23** (1981) 2571.

[Ra89] S. Raman et al. At. Data Nucl. Data Tables **42** (1989)1; and S. Raman et al. At. Data Nucl. Data Tables **36** (1987)1.

[Ra94] J. Rapaport and E. Sugarbaker, Ann. Rev. Nucl. Part. Sci. **44** (1994) 109.

[Rh80] M.J. Rhoades-Brown, M.H. Macfarlane and S.C. Peiper, Phys. Rev. **C21** (1980) 2417, 2436.

[Ri80] P. Ring and P. Schuck, The Nuclear Many Body Problem (Springer-Verlag,1980)

[Ri93] J. Ritman, F.D. Berg, W. Kühn, V. Metag, R. Novotny, M. Notheisen, P. Paul, M. Pfeiffer, O. Schwalb, H. Löhner, L. Venema, A. Gobbi, N. Herrmann, K.D. Hildenbrand, J. Mösner, R.S. Simon, K. Teh, J.P. Wessels and T. Wienold, Phys. Rev. Lett. **70** (1993) 533.

[Ro85] P. Roussel, N. Alamanos, F. Auger, J. Barrette, B. Berthier, B. Fernandez, L. Papineau, H. Doubre, and W. Mittig, Phys. Rev. Lett. **54** (1985) 1779.

[Ro88] P. Roussel-Chomaz, N. Alamanos, F. Auger, J. Barrette, B. Berthier, B. Fernandez, L. Papineau, H. Doubre, and W. Mittig, Nucl. Phys. **A477** (1988) 345.

[Sa73] G. R. Satchler, Comments Nucl. Part. Phys. **6** (1973) 105.

[Sa79] G.R. Satchler and W.G. Love, Phys. Rep. **55** (1979) 183.

[Sa83] G.R. Satchler, Direct Nuclear Reactions (Oxford Univ. Press, Oxford, 1983)

[Sa83b] R. Sartor and Fl. Stancu, Nucl. Phys. **A404** (1983) 392.

[Sa84] Y. Sakuragi and M. Kamimura, Phys. Lett. **149B** (1984) 307.

[Sa86] Y. Sakuragi, Phys. Rev; C35 (1987) 2161 and Y. Sakuragi, M. Yahiro and M. Kamimura, Prog. Theor. Phys. Suppl. **89**, 136 (1986).

[Sa87] G.R. Satchler, Nucl. Phys. **A472** (1987) 215.

[Sa94] G.R. Satchler, Nucl. Phys. **A579** (1994) 241.

[Sc93] R. Schmidt, Th. Blaich, Th.W. Elze, H. Emling, H. Freiesleben, K. Grimm, W. Henning, R. Holtzmann, J.G. Keller, H. Klingler, R. Kulessa, J.V. Kratz, D. Lambrecht, J.S. Lange, Y. Leifels, E. Lubkiewicz, E.F. Moore, E. Wajda, W. Prokopowicz, Ch. Schütter, H. Spies, K. Stelzer, J. Stroth, W. Walus, H.J. Wollersheim, M. Zinser, and E. Zude, Phys. Rev. Lett. **70** (1993) 1767.

[Sc93a] J.A. Scarpaci, Y. Blumenfeld, Ph. Chomaz, N. Frascaria, J.P. Garron, J.C. Roynette, T. Suomijärvi, N. Alamanos, B. Fernandez, A. Gillibert, A. Lepine, and A. van der Woude, Phys. Rev. Lett. **71** (1993) 3766.

[Sh93] S. Shlomo, and D.H. Youngblood, Phys. Rev. **C47** (1993) 529.

[Sp91] J. Speth, Inter. Rev. of Nucl. Phys. **V7** (1991). (Wold Scientific Edited by J. Speth).

[Sp89] R.H. Spear, At. Data Nucl Data Tables 42 (1989) 55.

[St79] R.G. Stokstad, R.M. Wieland, G.R. Satchler, C.B. Fulmer, D.C. Hensley, S. Raman, L.D. Rickertsen, A.H. Snell, and P.H. Stelson, Phys. Rev **C20** (1979) 655.

[Su89] T. Suomijärvi, D. Beaumel, Y. Blumenfeld, Ph. Chomaz, N. Frascaria, J.P. Garron, J.C. Jacmart, J.C. Roynette, J. Barrette, B. Berthier, B. Fernandez, J. Gastebois, P. Roussel-Chomaz, W. Mittig, L. Kraus and I. Linck, Nucl. Phys. A491 (1989) 314.

[Ta56] L.J. Tassie, Austral. J. Phys. 9 (1956) 407.

[Ta87] T.N. Taddeucci, C.A. Goulding, T.A. Carey, R.C. Byrd, C.D. Goodman, C. Gaarde, J. Larsen, D. Horen, J. Rapaport, and E. Sugarbaker, Nucl. Phys. **A469** (1987) 125.

[Ta88] I. Tanihata, T. Kobayashi, O. Yamakawa, S. Shimoura, K. Ekuni, K. Sugimoto, N. Takahashi, T. Shimoda, and H. Sato, Phys. Lett. **B206** (1988) 592.

[Th88] I. J. Thompson, Comp. Phys. Rep. 7 (1988) 167.

[To90] Y. Toba, Y.W. Lui, D.H. Youngblood, U. Garg, P. Grabmayr, K.T. Knöpfle, H. Riedesel and G.J. Wagner, Phys. Rev. **C41** (1990) 1417.

[Tr94] C. Troncy-Fortier Rapport de stage CEA/DAPNIA/SPhN 94 41.

[Va90] A.C. Vasconcellos Gomes and C.A. Bertulani, Nucl. Phys. **A571** (1990) 639.

[Va91] R. L. Varner, W.J. Thompson, T.L. McAbee, E.J. Ludwing, and T.B. Clegg, Phys. Rep. **201** (1991) 57.

[Wo87] A. Van der Woude, Prog. in Part. and Nucl. Phys. **18** (1987) 217.

[Wo91] A. Van der Woude, Inter. Rev. of Nucl. Phys. **V7** (1991) 99. (Wold Scientific, Edited by J. Speth).

[Wu79] P. Wust, W. von Oertzen, H. Ossenbrink, H. Lettau, H.G. Bohlen, W. Saathoff and C.A. Wiedner, Z. Phys. **A291** (1979) 151.

[Yo81] D.H. Youngblood, P. Bogucki, J.D. Bronson, U. Garg, Y.W. Lui, and C.M. Rozsa, Phys. Rev. **C23** (1981) 1997.